

## Reply to reviewers and editors:

We thank all reviewers for their careful reading of the manuscript, and for their many constructive feedbacks. The original comments by reviewers are in black font, our replies are in blue.

### Reviewer #1

This paper presents the formulation and sensitivity analysis for the inverse modeling of SO<sub>2</sub> and NO<sub>x</sub> emission over China using satellite data. While the authors seem to emphasize that the joint assimilation saves 50% of the computational time than assimilating SO<sub>2</sub> and NO<sub>2</sub> separately, the benefit of the joint assimilation should be more than that. This needs to be clarified.

Thanks for your comment. Yes, joint inversion should have more benefits in addition to save computational time. We have added the discussion below to Sect. 4.3.

When evaluating with OMI retrievals, joint inversion shows better results than separate inversion for SO<sub>2</sub> or NO<sub>2</sub>, but not both, depending on the value of  $\gamma$ . When  $\gamma$  is 20, 50, or 100, NO<sub>2</sub> NCRSME for E-joint-d $\gamma$  improvement appears to be smaller than that for E-NO<sub>2</sub>, but SO<sub>2</sub> NCRSME for E-joint-d $\gamma$  is larger than that for E-SO<sub>2</sub>. Conversely, when  $\gamma$  is 1000, 1500, or 2000, SO<sub>2</sub> NCRSME for E-joint-d $\gamma$  is smaller than that for E-SO<sub>2</sub>, but NO<sub>2</sub> NCRSME for E-joint-d $\gamma$  is larger than that for E-NO<sub>2</sub>. This is similar to the findings by Qu et al., (2019b) in which the months when joint inversion show better result than separate inversion for SO<sub>2</sub> (NO<sub>2</sub>) have worse result for NO<sub>2</sub> (SO<sub>2</sub>). The benefit of joint inversion for improving only one species is similar to Qu et al. (2019b) and is likely to due to the complicated relationship between these two species through different chemical pathways. For example, O<sub>3</sub> and OH are key species that connect the chemistry of SO<sub>2</sub> and NO<sub>2</sub> and aerosols can affect the photolysis and heterogenous chemistry. Hence, while joint inversion to improve both species can not be demonstrated here, it should be reviewed as the first step of simultaneously assimilating multiple species (including AOD, NH<sub>3</sub>, and other trace gases) to optimize emissions. Until then, the system is not ready to holistically evaluate the benefits of joint assimilation to improve the model in a systematic manner. It is worthy noting that Xu et al. (2013) showed the feasibility of using MODIS cloud-

free radiance to optimize emissions of SO<sub>2</sub> and NO<sub>2</sub> at the same time. Future research should add the aerosol optical depth or visible reflectance (as well as tropospheric O<sub>3</sub> if reliable) as constraints to further evaluate the benefits of joint assimilation for improving model overall performance in a systematic matter.

In the paper,  $\gamma$  is introduced to balance the SO<sub>2</sub> and NO<sub>2</sub> terms. In theory, it is not needed if the uncertainty terms can be well quantified. The optimal value of  $\gamma$  is determined pretty arbitrarily. There are objective ways (such as Hollingworth-Lönnberg and NMC methods) to determine the observational errors and its covariance terms instead of relying on arbitrary balancing.

Thank you for the comments. In a practical way, we still need use  $\gamma$  to balance the SO<sub>2</sub> and NO<sub>2</sub> terms no matter how observational errors are quantified, as “When it is not balanced, SO<sub>2</sub> observations have very little impact on the inversion results as the optimization algorithm will firstly minimize the observational term for NO<sub>2</sub> unless many more iterations than is computationally feasible are performed, which is caused by the fact that observational error and valid number of NO<sub>2</sub> observation are respectively smaller and larger than the counterparts of SO<sub>2</sub>. We thus **subjectively** derive  $\gamma$  in a **non-arbitrary** way in order to focus equally on both species, thereby tackling the imbalance in their observational constraints. In this manner, the cost function is defined to server the purpose of joint inversion of SO<sub>2</sub> and NO<sub>2</sub> emissions” “Similar balance approach that adjusts contribution of observation terms in the cost function is used in the past work that assimilates satellite trace gas retrievals to invert emissions (Qu et al., 2019b) or invert the aerosol optical properties from skylight polarization measurements of AERONET (Xu et al., 2015).” We have added the quoted text to Sect. 3.2.1.

Actually, OMPS SO<sub>2</sub> and NO<sub>2</sub> observational errors are quantified in an **objective** way. In a clean region (such as equatorial Pacific ocean (10°S–10°N, 120°W–150°W) that is far from emission sources), true SO<sub>2</sub> (NO<sub>2</sub>) concentrations should be zero or negligible, while both negative and positive retrieval values exist. Thus, it is reasonable to use the variance of SO<sub>2</sub> (NO<sub>2</sub>) retrievals over the clean region to represents SO<sub>2</sub> (NO<sub>2</sub>) observation error variance. This error estimation approach is widely used in trace gas retrieval research community (Li et al.,

2013; Yang et al., 2013). These precision values can be used as the observation error in the cost function of data assimilation. However, we should notice that the estimated observation (retrieval) errors only represent the observation error distribution of the products as a whole; it cannot represent the observation error distribution for every pixel, because the pixel-level error is amenable to spatiotemporal change of cloud fraction, satellite observation geometry, aerosol impacts, etc. In theory, if the uncertainties can be analytically described at the pixel level, they would be directly applied to improve the satellite product in the first place.

We have added the discussion above in Sect. 2.1.

We also have added the text below in Sect. 3.1

In the optimization formulation, the forward model errors are also considered as part of the observation error term. However, while several ways to construct model error covariance matrix exist, including the Hollingworth-Lönnberg (Hollingsworth & Lönnberg, 1986) and NMC (Bannister, 2008) methods, their application for off-line CTM model error characterization deserves a separate study. The Hollingsworth method extracts observation error variance (including forward model error) from (observation – background) covariance statistics with the assumptions that observation error is spatially uncorrelated, background error is spatially correlated as a function of distance, and observation error and background error are uncorrelated. The assumption that background error is spatially correlated as a function of distance only is suitable for the meteorological fields that vary smoothly, but for chemical species, emissions also contribute significantly to model errors and emissions are spatially correlated. The NMC method is normally applied to weather forecast models or on-line-coupled weather-chemistry models (Benedetti and Fisher, 2007). Off-line CTMs such as GEOS-Chem use the meteorological reanalysis and so, NMC is not applicable here to quantify the CTM's transport error. Consequently, CTM's transport errors are neglected in the past emission optimization work (Wang et al., 2016) and are adopted in this study. Admittedly, this simplification should be studied in future together with the evaluation and developments of methods to characterize off-line CTM errors.

***Specific comments:***

Line 215: It is surprising for the authors to choose less than 3% reduction in the cost function between two iterations as a criterion to halt the minimization. The L-BFGS-B can be very slow. Such a condition can often terminate the minimization prematurely. This needs to be changed if it is not a typo.

This is a good point. L-BFGS-B can be very slow to converge. But at some point we run into practical limitations on the amount of time we can spend iterating, thus we choose less than 3% reduction in the cost function between two successful iterations as a criterion to halt the minimization. Based on the criterion, for E-SO<sub>2</sub> and E-NO<sub>2</sub>, we picked 5<sup>th</sup> and 6<sup>th</sup> iteration result, respectively. Further tests show that the more iterations (after <3% reduction of cost function) doesn't yield discernable difference in the cost function values (Fig. S3) and optimization results (Table S1 and S2). We have added the figure and table below to the supplement and added corresponding description at last paragraph of Sect. 3.1.

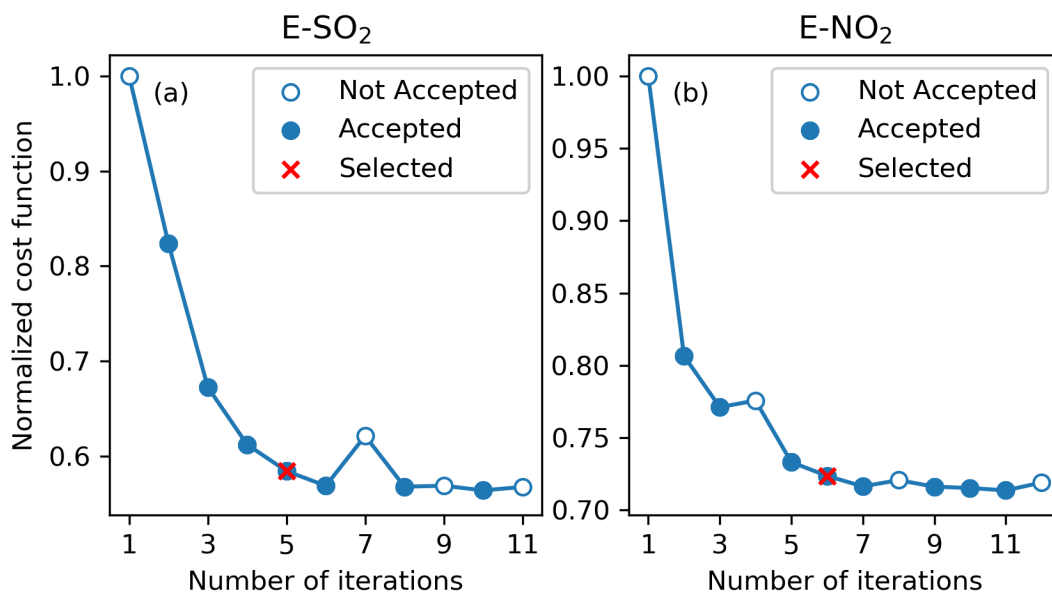


Figure S3. Normalized cost function (the ratio of the cost function at a iteration to that at the 1<sup>st</sup> iteration) for E-SO<sub>2</sub> (a) and E-NO<sub>2</sub> (b). A iteration is accepted (solid circle) if its cost function value is smaller than that of any previous iterations, otherwise not accepted (empty circle). The 1<sup>st</sup> iteration (prior) is defined as not accepted. The iterations that are selected based on the halt criterion are marked with red cross.

**Table S1. Anthropogenic SO<sub>2</sub> emissions for October 2013 from E-SO<sub>2</sub> at each iteration.**

Iteration	1 (prior)	5 (selected)	6	7	8	9	10	11
SO <sub>2</sub> [Gg S]	1166	748	744	Not accepted <sup>a</sup>	746	Not accepted	749	Not accepted

<sup>a</sup>Posterior emission total amount at the iteration that is not accepted (cost function value is not smaller than that of any previous iterations) is not shown.

**Table S2. Anthropogenic NO<sub>x</sub> emissions for October 2013 from E-NO<sub>2</sub> at each iteration.**

Iteration	1 (prior)	6 (selected)	7	8	9	10	11	12
NO <sub>x</sub> [Gg N]	714	672	667	Not accepted <sup>a</sup>	666	666	666	Not accepted

<sup>a</sup>Posterior emission total amount at the iteration that is not accepted (cost function value is not smaller than that of any previous iterations) is not shown.

Lines 234-7: Is it really beneficial to balance the cost function this way? Can the SO<sub>2</sub> observation errors be objectively determined?

As we address that comment about using  $\gamma$  to balance observation term, SO<sub>2</sub> observation error is **objectively** determined, but the spatial balance problem still exists. Similar balance approach that adjusts contribution of observation terms in the cost function is used in the past work that assimilates satellite trace gas retrievals to invert emissions (Qu et al., 2019b) or invert the aerosol optical properties from skylight polarization measurements of AErosol RObotic NETwork (AERONET) (Xu et al., 2015). Thus we think the subjective but non-arbitrary balance approach should be acceptable, although it is a break from strict Bayesian derivation of the cost function. We have added how the SO<sub>2</sub> observation error (0.2 DU) are determined in an objective way in Sect. 2.1 and the justification of the balance approach in Sect. 3.2.1.

Line 247: It is not accurate to say “emissions are adjusted mainly at locations where prior emissions are large”. If there are non-zero emissions, the adjustments can be made. The limitation of using scaling factors is that zero-emission grid points cannot be modified.

Yes. We agree that “The limitation of using scaling factors is that zero-emission grid points cannot be modified.” We have added statement of the limitation in the manuscript.

***Technical correction:***

Line 161, "Terrain reflectivity less than 30o": Which angle does "Terrain reflectivity" refer to?

This is a typo. We have change it to "terrain reflectivity less than 0.3".

Line 171: GOES-FP -> GEOS-FP

Corrected.

Line 433: compared the latter -> compared with the latter

Corrected.

## Reply to reviewers and editors:

We thank all reviewers for their careful reading of the manuscript, and for their many constructive feedbacks. The original comments by reviewers are in black font, our replies are in blue.

### Reviewer #2

This manuscript presents joint inversion results of SO<sub>2</sub> and NO<sub>x</sub> emissions over China using the GEOS-Chem adjoint model and OMPS satellite observations for October 2013. The inversion results were compared against assimilated OMPS observations and independent OMI observations. Several sensitivity calculations were conducted to optimize the joint inversion framework. The joint inversion approach is unique, while the comparison against the OMI observations is interesting. I would, however, advise the authors to revise the manuscript. These revisions should be made before the manuscript can be considered for publication in ACP.

Thanks for the positive comments. We did our best to address them in the revision.

### *[ Major comments ]*

The model horizontal resolution (2°x2.5° resolution) is clearly too coarse for current regional (not global) emission research, which could lead to serious problems for many applications (e.g., systematic biases in the downscaling analysis (Part 2)). In the previous study by the author's group (Qu et al, 2019), regional Chinese regional emissions were estimated at 0.5°x0.667° resolution using a hybrid 4D-Var/Mass balance approach to save computational resources for the multiple-year calculations, while conducting a one-month adjoint calculation at 0.5°x0.667° resolution using the same adjoint model with a nested domain for East Asia. In the same way, one-month inversion calculation at 0.5°x0.667° resolution using OMPS observations must be doable and should be tested in the present study. This is essential for evaluating the joint inversion performance using in-situ observations (please see my comment below), as already performed by Qu et al. (2019) for OMI assimilation results. It could also provide improved information (e.g., reduced systematic errors for each grid point, considering the non-linear chemistry) for down-scaling analysis (Part 2). For long-term emission estimations, the authors could still use the hybrid inversion framework at 0.5°x0.667° resolution (together with the

downscaling approaches, if resolutions higher than at  $0.5^\circ \times 0.667^\circ$  resolution are needed). Thus, I don't think the coarse resolution regional joint inversion will be needed for any applications. At the very least,  $0.5^\circ \times 0.667^\circ$  resolution joint inversion calculations should be performed for key experiments.

Thanks for the good suggestions. We acknowledge that it is better to optimize emissions directly at fine resolution (such as  $0.5^\circ \times 0.667^\circ$ , and  $0.25^\circ \times 0.3125^\circ$ ) rather than coarse resolution (such as  $2^\circ \times 2.5^\circ$ ), and that it is doable for one-month inversion at fine resolution. After careful consideration, we think it is both practical and reasonable to assimilate OMPS retrievals at the resolution of  $2^\circ \times 2.5^\circ$ , as OMPS pixel size could be much larger than fine-resolution grid boxes (and OMI whose pixel size is 13 km x 24 km at nadir and 26 km x 128km at edge). OMPS pixel size is 50 km x 50 km at nadir, and becomes 190 km x 50 km at edges. Thus, OMPS pixel size is comparable to (at nadir) or much larger than (at edges)  $0.5^\circ \times 0.667^\circ$  grid box. An OMPS pixel may cover several  $0.5^\circ \times 0.667^\circ$  grid boxes and cannot resolve variations of concentrations owing to variations emissions at that fine resolution. Currently, the nested GOES-Chem adjoint model only supports the  $0.5^\circ \times 0.667^\circ$  GEOS-5 meteorological field and the  $0.25^\circ \times 0.3125^\circ$  GEOS-FP meteorological field. And the GEOS-5 meteorological field has a temporal coverage from 2004 to mid-2013; data after mid-2013, e.g., our study time period, is unavailable. Although  $0.25^\circ \times 0.3125^\circ$  GEOS-FP meteorological field is up to date, apparently its resolution is too fine to compare with OMPS. We have added this explanation in Sect. 3.2.

The joint inversion results, including those from the sensitivity calculations, need to be evaluated against independent in-situ measurements, in order to obtain the optimized system. For this, the authors need to use their  $0.5^\circ \times 0.667^\circ$  resolution joint inversion system. Resolutions higher than  $0.5^\circ \times 0.667^\circ$  would be required for reducing representation gaps, as discussed in Part 2.

Nevertheless, Qu et al (2019) already demonstrated that joint inversions at  $0.5^\circ \times 0.667^\circ$  resolution can be evaluated using in-situ surface observations. This is also essential for evaluating possible biases in both OMPS and OMI satellite observations, which can be one of the most important results from the present study.

As answered the previous question, due to large pixel size of OMPS, we didn't attempt to constrain the emissions at the resolution finer than the satellite instrument on the monthly basis. In addition, for those retrievals at high resolution (such as TROPOMI), the retrieval uncertainty is expected to



be alleviated after aggregating pixel-level retrieval into the coarser resolution. Furthermore, even if the inversion were conducted at the resolution of  $0.5^\circ \times 0.667^\circ$  or  $0.25^\circ \times 0.3125^\circ$ , it is still very challenging to evaluating possible bias in both OMPS and OMI satellite observations, as representation gaps still exists in the two resolutions. Zheng et al. (2017) showed that surface  $\text{SO}_2$  ( $\text{NO}_2$ ) concentration simulations from WRF-CMAQ, when evaluating with in situ observations, have a NMB of -23% (0%), 7% (32%), and 41% (45%) at the resolutions of 36 km ( $\sim 0.36^\circ$ ), 12 km ( $\sim 0.12^\circ$ ), and 4 km ( $\sim 0.04^\circ$ ), respectively; this shows that representation gaps still exist at 12 km ( $\sim 0.12^\circ$ ), which is already finer than  $0.5^\circ$  and  $0.25^\circ$ . Thus, perhaps it is not surprising that large negative bias exists when evaluating posterior GEOS-Chem  $0.5^\circ \times 0.667^\circ$  simulations with in situ  $\text{SO}_2$  (Fig. 10 in Qu et al. (2019)) and  $\text{NO}_2$  (Fig. 11 in Qu et al. (2019)) in Qu et al. (2019), and it is somewhat assertive to conclude that the negative bias imply the negative bias of OMI  $\text{SO}_2$  and  $\text{NO}_2$  retrievals. In Qu et al. (2019), the improvements of posterior simulations when evaluating with in situ  $\text{SO}_2$  and  $\text{NO}_2$  surface concentrations are mainly represented by Normalized Mean Square Error (NMSE) rather than bias.

The goal of this paper is NOT to replicate the method by Qu et al. (2019). Rather, the goal of this paper is to illustrate how OMPS data could be used to improve an air quality *forecast* through monthly update of emissions (possibly in near real time manner) at a resolution much finer than OMPS. Hence, if implemented, our method of using  $2^\circ \times 2.5^\circ$  resolution for performing the optimization can save considerable computational time (and is much more feasible for a research group such us in the university), and then using the downscaling method (part II developed by this study), the finer resolution forecast can be made in a practical manner (suitable for a regional modeling group for air quality forecast). In contrast, the focus of Qu et al (2019) is the re-analysis of emissions, as opposed to forecasting of air quality at the finer scales. In contrast, optimization at  $0.5^\circ \times 0.67^\circ$  will still require downscaling method for air quality forecast (normally at  $\sim 10$  km resolution). We have added the elaborations above in section 3.2.

Although the joint inversion reduced the total computational cost, its scientific benefits (required for ACP, not for GMD) are not very clear. The discussions in Sections 4.4 and 4.5 are

interesting. Adding evaluations using any AOD, NH<sub>3</sub>, and relevant observations would be helpful to demonstrate the scientific value of the joint inversion.

We have expanded discussion of the scientific benefits of the approach in response to the first comment from the reviewer 1, see above. Further, ACP's scope is very broad and developing data assimilation techniques for using new satellite data has been published in ACP, such as Chen et. al (2018). Please look at this part I and part II paper as a whole – they effectively showcase an approach that is economic in computation to use OMPS data to improve air quality forecast at fine scale. In part II, we did many independent evaluations. Furthermore, we also studied the results of the sensitivity to NH<sub>3</sub> – a topic that has not been studied before in data assimilation. We consider they have good scientific merits.

***[ A few more specific comments ]***

L203 “In this study, OMPS SO<sub>2</sub> and NO<sub>2</sub> tropospheric VCDs are retrieved using the shape of NO<sub>2</sub> vertical profiles from GEOS-Chem simulations (Yang et al., 2013; Yang et al., 2014), although differences of model version, simulation year, and emission inventory still exists”  
These profiles can be largely different. The lack of averaging kernel in the observation operator can lead to serious problems. Please justify and demonstrate its impacts. Otherwise, data assimilation adjustments can be meaningless.

Thanks for pointing out this. We totally agree that differences of model version, simulation year, and emission inventory could lead to profile differences. Thus, we compare operational OMPS retrievals with VCDs modified through averaging kernel to investigate how much VCD differences are caused by profile differences. We have added the discussion below to Sect. 4.1.1 and figures below to supplement.

For SO<sub>2</sub>

The SO<sub>2</sub> NMB (106.5%) between GOES-Chem prior simulation and OMPS is much larger than the NMB (-6.8%, Fig S1) caused by the difference of SO<sub>2</sub> vertical profiles between OMPS SO<sub>2</sub> retrieval algorithm and current prior simulation; thus averaging kernel is not considered in the OMPS SO<sub>2</sub> observation operator.

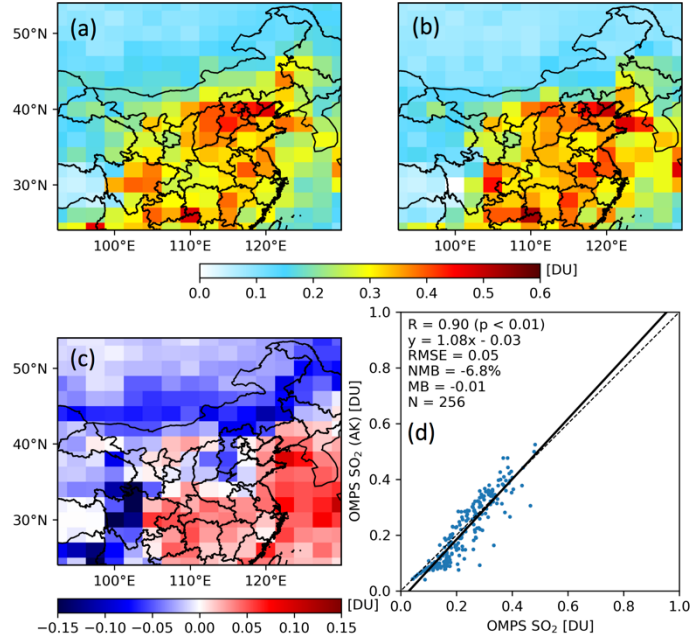


**Figure S1. OMPS SO<sub>2</sub> Vertical Column Density (VCD) retrievals in April 2018. (a) and (b) are operational VCDs and the VCDs that are modified through averaging kernel according to formula S1, respectively. (c) is the differences between the modified and operational VCDs. (d) is scatter plot of modified VCDs versus operational VCDs. Linear correlation coefficient (R), linear regression equation, root mean squared error (RMSE), normalized mean bias (NMB), mean bias (MB), and number of observations (N) are shown over the scatter plot.**

For NO<sub>2</sub>

Similarly, the averaging kernel is not considered in the OMPS NO<sub>2</sub> observation operator for optimization for the following reasons. First, the OMPS NO<sub>2</sub> retrieval differences due to the profile differences can lead to a NMB of -7.5% (Fig S2), which is still smaller than the prior GEOS-Chem simulation NMB (10.9%, Fig. 31). Second, a NMB of 10.9% for model NO<sub>2</sub> VCD simulation is not a very large value, as the difference between satellite NO<sub>2</sub> VCD retrievals and ground-based measurements could be comparable to this value. For example, Krotkov et al. (2017) shows that OMI NO<sub>2</sub> VCD retrievals, on average, are ~10% larger than ground-based FTIR spectrometer. Thus, current research should mainly focus on the change of the spatial distribution (such as linear correlation coefficient) rather than bias of prior and posterior GEOS-Chem NO<sub>2</sub> VCD simulation. Finally, given that linear correlation coefficient between OMPS retrievals and that are modified through integration of averaging kernel and NO<sub>2</sub> vertical profile from this study is as large as 0.99, averaging kernel is not treated in the OMPS NO<sub>2</sub> observation operator.

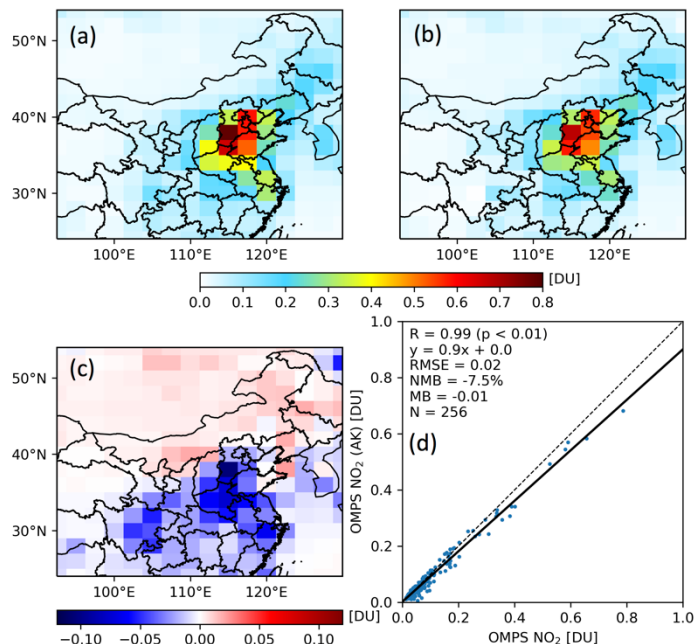


**Figure S2. OMPS NO<sub>2</sub> Vertical Column Density (VCD) retrievals in October 2013. (a) and (b) are operational VCDs and the VCDs that are modified through averaging kernel according to formula S1, respectively. (c) is the differences between the modified and operational VCDs. (d) is scatter plot of modified VCDs versus operational VCDs. Linear correlation coefficient (R), linear regression equation, root mean squared error (RMSE), normalized mean bias (NMB), mean bias (MB), and number of observations (N) are shown over the scatter plot.**

L204 “Hence, the difference between the GEOS-Chem simulations and the OMPS retrievals is mostly ascribed to the uncertainty of the emissions.” This may not be true and requires further investigation.

We acknowledge that when averaging kernel is not considered in the observation operator, the profile differences can contribute to the difference between the GEOS-Chem simulations and the OMPS retrievals. Additionally, GEOS-Chem model uncertainty can also contribute to the difference between the GEOS-Chem simulations and the OMPS retrievals, and it is difficult to estimate model uncertainty. Thus, we delete the sentence in the revised manuscript; we added the discussion in Sect. 4.1.1 to show that difference between the GEOS-Chem simulations and the operational OMPS retrievals is larger than difference between operational OMPS retrievals and retrievals modified through consideration of averaging kernel. Therefore, the inverse modeling results are statistically significant. We also acknowledge that GEOS-Chem model uncertainty affects inverse modeling results, thus we apply optimized emission inventory to another model (different version of the GEOS-Chem model with much finer resolution) to show that improvement of air quality simulation and forecasts is obtained though the uncertainty of

models. In addition, we also follow the suggestion of evaluating the optimized emission inventory in a consistent framework for part II manuscript; please see details in our reply for part II manuscript.

OMI L3 data is used for validation. Without applying the averaging kernels, comparisons may not provide meaningful information. This needs to be investigated.

Thanks for the suggestion. We acknowledge there should be differences between apply and do not apply averaging kernels (or scattering weights) in the comparisons. Following the suggestion, we investigate how this affect evaluation. In the manuscript, OMI L3 SO<sub>2</sub> and OMI L3 NO<sub>2</sub> are used for evaluation. In OMI L3 SO<sub>2</sub> dataset, only the best pixel in a 0.25°x0.25° grid cell is retained, and the observational geometry information for the pixel is also available. Thus, we can still apply scattering weights to OMI L3 SO<sub>2</sub>. In OMI L3 NO<sub>2</sub> dataset, observational geometry information it not available, thus we can only apply scattering weights to OMI L2 NO<sub>2</sub>. The text and figures below are added to supplement. We have emphasized in the main text that these conclusions do not change in Sect. 4.1.3.

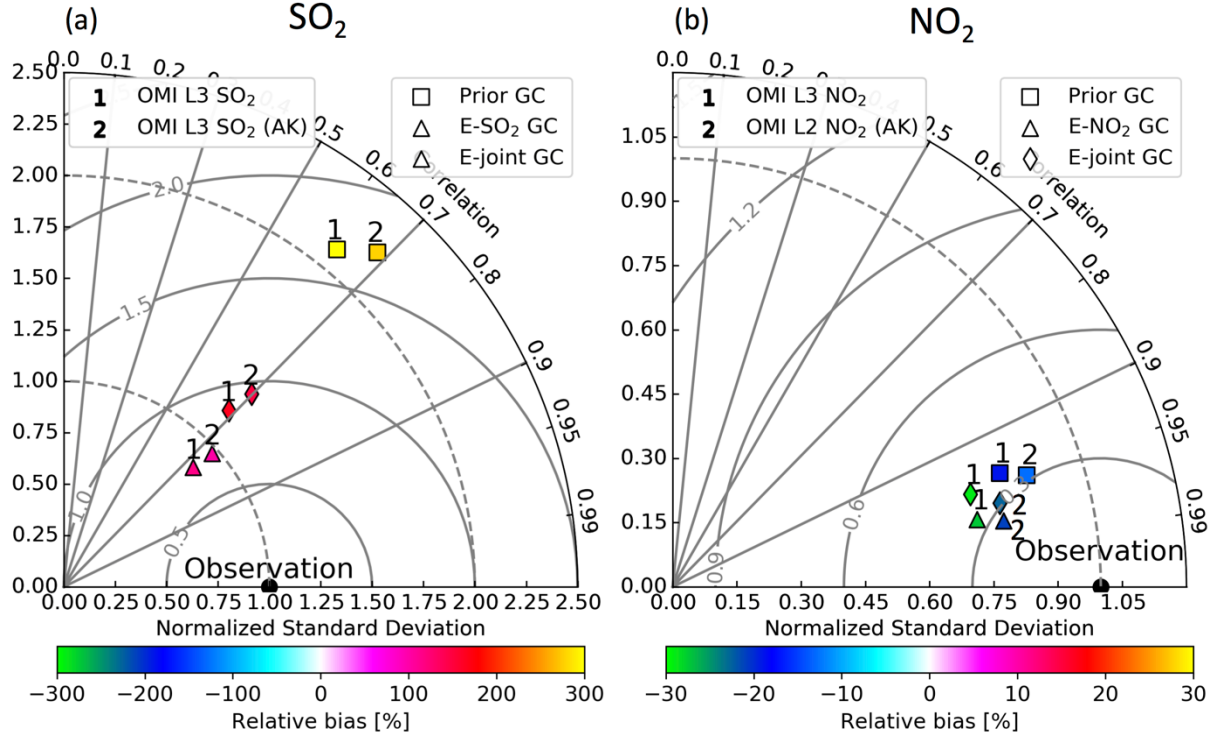


Figure S4. Taylor diagrams for comparing of VCDs of SO<sub>2</sub> (a) and NO<sub>2</sub> (b) from the GEOS-Chem simulations (squares for prior, triangles for posterior E-SO<sub>2</sub> (a) or E-NO<sub>2</sub> (b), and diamonds for E-joint) with that from the OMI (label 1 for operational level 3 SO<sub>2</sub> (a) or level 3 NO<sub>2</sub> (b) and label 2 for the level 3 SO<sub>2</sub> (a) that are modified by considering the vertical profiles from the GEOS-Chem simulation with which is to be compared or the level 2 NO<sub>2</sub> (b) that are modified by considering the vertical profiles from the GEOS-Chem simulation with which is to be compared) in October 2013 over China.

$$\Omega_s^{opl} = \Omega_v^{opl} \cdot M^{opl} \quad (S2)$$

$$M^{new} = \frac{S^{new}}{S^{opl}} \quad (S3)$$

$$\Omega_v^{opl} = \frac{\Omega_s^{opl}}{M^{new}} \quad (S4)$$

Equation S2 is used to convert OMI SO<sub>2</sub> (NO<sub>2</sub>) vertical column density  $\Omega_v^{opl}$  to SO<sub>2</sub> (NO<sub>2</sub>) slant column density  $\Omega_s^{opl}$  by multiplying SO<sub>2</sub> (NO<sub>2</sub>) air mass factor  $M^{opl}$  from OMI product. Equation S3 is used to calculate new SO<sub>2</sub> (NO<sub>2</sub>) air mass factor  $M^{new}$ , where  $\mathbf{W}$  is SO<sub>2</sub> (NO<sub>2</sub>) scattering weight, and  $S^{new}$  is SO<sub>2</sub> (NO<sub>2</sub>) shape factor that from the GEOS-Chem simulation with which is to be compared. Equation S4 is used to calculate new OMI SO<sub>2</sub> (NO<sub>2</sub>) vertical column density  $\Omega_v^{opl}$ .

Whether use OMI data without applying scattering weight (Label 1 in Fig. S4) or OMI data with applying scattering weight (Label 2 in Fig. S4), the main conclusions in Sect. 4.1.3 does not change. These conclusions are:

- (1) For SO<sub>2</sub>, posterior GEOS-Chem simulations (E-SO<sub>2</sub> and E-joint) show smaller NMB and better spatial distribution (in terms of NCRMSE) than prior GEOS-Chem simulations when evaluating with OMI SO<sub>2</sub> (apply or not apply scattering weight).
- (2) For NO<sub>2</sub>, the improvements for E-NO<sub>2</sub> and E-joint are reflected in terms of R when evaluating with OMI tropospheric VCDs (apply or not apply scattering weight), although the two experiments show larger negative NMB than the prior simulation.

L325 and some other places, “Our finding of a large reduction. . .“ The discussion about trends between the 2013 October inversion and the 2010 inventories does not make any sense.

Thanks for pointing out this. The MIX 2010 inventory was derived through bottom-up approach, while the 2013 October inversion inventory is derived through integration of GEOS-Chem adjoint model and OMPS SO<sub>2</sub> and NO<sub>2</sub> vertical column density retrievals. We have to acknowledge that systematic bias exists in both of the inventories, and so, the difference between the two emission inventories should not be considered as trend. To investigate trends, emission inventories should be derived from the same approach. In the revision, we therefore have removed the discussions and emphasized that the differences should not be considered as trends.

L330 “in some model grid cells”: Please discuss the spatial pattern.

Sure. We have added “Although the relative difference between E-joint and E-NO<sub>2</sub> proved to be less than 2% in terms of total anthropogenic NO<sub>x</sub> emissions over China (Fig. 4k), it is up to 40% over Shanxi province, and both grids with large positive differences and grids with large negative differences exist over North China Plain (Fig. 4 l).” in section 4.1.2.

Section 4.2 does not provide very useful information and can be removed or shortened.

Thank you for the comment. This section shows the impacts of data quality control and spatial balance. Although it does not include much scientific information, it helps to understand how observational errors are assumed. Thus, we hope to keep it.

## Reference

- Bannister, R. N.: A review of forecast error covariance statistics in atmospheric variational data assimilation. I: Characteristics and measurements of forecast error covariances, *Quarterly Journal of the Royal Meteorological Society*, 134, 1951-1970, 10.1002/qj.339, 2008.
- Chen, C., Dubovik, O., Henze, D. K., Lapyonak, T., Chin, M., Ducos, F., Litvinov, P., Huang, X., and Li, L.: Retrieval of desert dust and carbonaceous aerosol emissions over Africa from POLDER/PARASOL products generated by the GRASP algorithm, *Atmos. Chem. Phys.*, 18, 12551–12580, <https://doi.org/10.5194/acp-18-12551-2018>, 2018.
- Hollingsworth, A., and Lönnberg, P.: The statistical structure of short-range forecast errors as determined from radiosonde data. Part I: The wind field, *Tellus A*, 38A, 111-136, 10.1111/j.1600-0870.1986.tb00460.x, 1986.
- Krotkov, N. A., Lamsal, L. N., Celarier, E. A., Swartz, W. H., Marchenko, S. V., Bucsela, E. J., Chan, K. L., Wenig, M., and Zara, M.: The version 3 OMI NO<sub>2</sub> standard product, *Atmos. Meas. Tech.*, 10, 3133-3149, 10.5194/amt-10-3133-2017, 2017.
- Li, C., Joiner, J., Krotkov, N. A., and Bhartia, P. K.: A fast and sensitive new satellite SO<sub>2</sub> retrieval algorithm based on principal component analysis: Application to the ozone monitoring instrument, *Geophys. Res. Lett.*, 40, 6314-6318, 10.1002/2013GL058134, 2013.
- Qu, Z., Henze, D. K., Theys, N., Wang, J., and Wang, W.: Hybrid Mass Balance/4D-Var Joint Inversion of NO<sub>x</sub> and SO<sub>2</sub> Emissions in East Asia, *J. Geophys. Res.*, 124, 8203-8224, 10.1029/2018JD030240, 2019.
- Xu, X., Wang, J., Henze, D. K., Qu, W., and Kopacz, M.: Constraints on aerosol sources using GEOS-Chem adjoint and MODIS radiances, and evaluation with multisensor (OMI, MISR) data, *J. Geophys. Res.*, 118, 6396-6413, 10.1002/jgrd.50515, 2013.
- Xu, X., Wang, J., Zeng, J., Spurr, R., Liu, X., Dubovik, O., Li, L., Li, Z., Mishchenko, M. I., Siniuk, A., and Holben, B. N.: Retrieval of aerosol microphysical properties from AERONET photopolarimetric measurements: 2. A new research algorithm and case demonstration, *J. Geophys. Res.*, 120, 2015JD023113, 10.1002/2015JD023113, 2015.
- Yang, K., Dickerson, R. R., Carn, S. A., Ge, C., and Wang, J.: First observations of SO<sub>2</sub> from the satellite Suomi NPP OMPS: Widespread air pollution events over China, *Geophys. Res. Lett.*, 40, 4957-4962, 10.1002/grl.50952, 2013.
- Zheng, B., Zhang, Q., Tong, D., Chen, C., Hong, C., Li, M., Geng, G., Lei, Y., Huo, H., and He, K.: Resolution dependence of uncertainties in gridded emission inventories: a case study in Hebei, China, *Atmos. Chem. Phys.*, 17, 921-933, 10.5194/acp-17-921-2017, 2017.



# Inverse modeling of SO<sub>2</sub> and NO<sub>x</sub> emissions over China using multi-sensor satellite data: 1. formulation and sensitivity analysis

5 Yi Wang<sup>1</sup>, Jun Wang<sup>1,2</sup>, Xiaoguang Xu<sup>2,3</sup>, Daven K. Henze<sup>4</sup>, Zhen Qu<sup>4</sup>, Kai Yang<sup>5</sup>

<sup>1</sup>Interdisciplinary Graduate Program in Informatics, The University of Iowa, Iowa City, IA 52242, USA

<sup>2</sup>Department of Chemical and Biochemical Engineering, and Center for Global & Regional Environmental Research, The University of Iowa, Iowa City, IA 52242, USA

<sup>3</sup>Joint Center for Earth Systems Technology and Department of Physics, University of Maryland Baltimore County, Baltimore, Maryland, 21250, USA

<sup>4</sup>Department of Mechanical Engineering, University of Colorado Boulder, Boulder, CO 80309, USA

<sup>5</sup>Department of Atmospheric and Oceanic Sciences, University Maryland, College Park, MD 20742, USA

15 *Correspondence to:* Jun Wang ([jun-wang-1@uiowa.edu](mailto:jun-wang-1@uiowa.edu)) and Yi Wang ([yi-wang-4@uiowa.edu](mailto:yi-wang-4@uiowa.edu))

**Abstract.** SO<sub>2</sub> and NO<sub>2</sub> observations from the Ozone Mapping and Profiler Suite (OMPS) sensor are used for the first time in conjunction with GEOS-Chem adjoint model to optimize both SO<sub>2</sub> and NO<sub>x</sub> emission estimates over China for October 2013. [Separate and joint \(simultaneous\) optimizations of SO<sub>2</sub> and NO<sub>2</sub> emissions are both conducted and compared.](#) Posterior emissions, compared to the prior, yield improvements in simulating columnar SO<sub>2</sub> and NO<sub>2</sub>, in comparison to measurements from OMI and OMPS. The posterior SO<sub>2</sub> and NO<sub>x</sub> emissions from separate inversions are 748 Gg S and 672 Gg N, which are 36% and 6% smaller than prior MIX emissions ([valid for 2010](#)), respectively. In spite of the large reduction of SO<sub>2</sub> emissions over the North China Plain, the simulated sulfate-nitrate-ammonium Aerosol Optical Depth (AOD) only decrease slightly, which can be attributed to (a) nitrate rather than sulfate as the dominant contributor to AOD and (b) replacement of ammonium sulfate with ammonium nitrate as SO<sub>2</sub> emissions are reduced. [For joint inversions, both data quality control and the weight given to SO<sub>2</sub> relative to NO<sub>2</sub> observations can affect the spatial distributions of the posterior emissions.](#) When the latter is properly balanced, the posterior emissions from assimilating OMPS SO<sub>2</sub> and NO<sub>2</sub> jointly yield a difference of -3% to 15% with respect to the separate assimilations for total anthropogenic SO<sub>2</sub> emissions and ±2% for total anthropogenic NO<sub>x</sub> emissions; but the differences can be up to 100% for SO<sub>2</sub> and 40% for NO<sub>2</sub> in some grid cells. Improvements on SO<sub>2</sub> and NO<sub>2</sub> simulations from the joint inversions are overall consistent with those from separate inversions. Moreover, the joint assimilations save ~50% of the computational time than assimilating SO<sub>2</sub> and NO<sub>2</sub> separately [in a sequential manner of computation.](#) The sensitivity analysis shows that a perturbation of

NH<sub>3</sub> to 50% (20%) of the prior emission inventory: (a) has negligible impact on the separate SO<sub>2</sub> inversion, but can lead to decrease of posterior SO<sub>2</sub> emissions over China by -2.4% (-7.0%) in total and up to -9.0% (-27.7%) in some grid cells in the joint inversion with NO<sub>2</sub>; (b) yield posterior NO<sub>x</sub> emissions over China decrease by -0.7% (-2.8%) for the separate NO<sub>2</sub> inversion and by -2.7% (-5.3%) in total and up to -15.2% (-29.4%) in some grid cells for the joint inversion. The large reduction of SO<sub>2</sub> between 2010 and 2013, however, only leads to ~10% decrease of AOD regionally; reducing surface aerosol concentration requires the reduction of emissions of NH<sub>3</sub> as well.

## 1. Introduction

Both SO<sub>2</sub> and NO<sub>2</sub> in the atmosphere have adverse impacts on human health and can affect radiative forcing that leads to climate change. Not only do they cause inflammation and irritation of the human's respiratory system, but they also react with other species to form sulfate and nitrate aerosols (Seinfeld and Pandis, 2016), which subsequently can lead to or exacerbate respiratory and cardiovascular diseases (Lim et al., 2012). Sulfate and nitrate account for the largest mass of anthropogenic aerosols, which contributed to ~3 million premature deaths worldwide in 2010 (Lelieveld et al., 2015). In addition to the health impacts, anthropogenic sulfate and nitrate particles are estimated to have caused -0.4 and -0.15 W m<sup>-2</sup> radiative forcing, respectively, on a global scale between 1750 and 2011 through scattering solar radiation, and via modifying cloud microphysical properties (Myhre et al., 2013).

Satellite-derived global distributions of SO<sub>2</sub> and NO<sub>2</sub> Vertical Column Densities (VCDs) have been used to study the aforementioned impacts of SO<sub>2</sub> and NO<sub>2</sub> on atmospheric composition, climate change, and human health. In particular, since SO<sub>2</sub> and NO<sub>2</sub> VCDs are, to first order, linearly related to SO<sub>2</sub> and NO<sub>x</sub> emissions (Calkins et al., 2016), they can be used to update bottom-up emission inventories that have large uncertainties and a temporal lag often of at least one year (Liu et al., 2018). Of particular interest for this study is China, which has large SO<sub>2</sub> and NO<sub>x</sub> emissions from anthropogenic sources (coal-fired power plants, industry, transportation, and residential activity). Moreover, China has seen a 62% reduction in anthropogenic SO<sub>2</sub> emissions and a 17% reduction of anthropogenic NO<sub>x</sub> emissions on average from 2010 to 2017 (Zheng et al., 2018) due to the implementation of emission control policies, and these changes vary by regions, cities (Liu et al., 2016), and sectoral sources (Zheng et al., 2018). The reduction of SO<sub>2</sub> emissions mainly occurred in the coal-fired power plants and industries while the decrease of NO<sub>x</sub> emissions was largely ascribed to coal-fired power plants (Zheng et al., 2018). Noticeable uncertainties larger than 30% for both anthropogenic SO<sub>2</sub> and NO<sub>x</sub> in 2010 over China were documented (Li et

al., 2017b) and can be larger at the regional scale due to the uncertainty of activity rates, emission factors, and spatial proxies, which are used in the bottom-up approach (Janssens-Maenhout et al., 2015). [The uncertainty is large and can be](#) compounded by possible discrepancies caused by the temporal lag of bottom-up emission  
65 inventories and the rapid changes of emissions over time.

Several methods have been developed to update SO<sub>2</sub> and NO<sub>x</sub> emissions using satellite VCD retrievals of SO<sub>2</sub> and NO<sub>2</sub>, which have global coverage and [allows](#) near-real-time access. The mass balance method, which scales  
70 prior emissions by the ratios of observed VCDs to Chemistry Transport Model (CTM) counterparts, was applied to SO<sub>2</sub> retrievals from SCanning Imaging Absorption SpectroMeter for Atmospheric CHartographyY (SCIAMACHY) and Ozone Monitoring Instrument (OMI) (Lee et al., 2011;Koukouli et al., 2018) and to NO<sub>2</sub> from Global Ozone Monitoring Experiment (GOME) and OMI (Martin et al., 2003;Lamsal et al., 2010) to estimate SO<sub>2</sub> and NO<sub>x</sub> emissions, respectively. Lamsal et al. (2011) simulated the sensitivity of VCDs to emissions  
75 (the finite difference mass balance approach) using a CTM, which was applied to OMI NO<sub>2</sub> retrievals to estimate NO<sub>x</sub> emissions. SO<sub>2</sub> VCD retrievals from GOME, GOME-2, SCIAMACHY, and Ozone Mapping and Profiler Suite (OMPS) were used to estimate point sources through linear regression between VCDs and emissions or function fitting, although the method can only detect about half of the total anthropogenic SO<sub>2</sub> emissions (Li et al., 2017a;Zhang et al., 2017;Fioletov et al., 2013;Fioletov et al., 2016). With explicit considerations of chemistry,  
80 transport, and deposition, the four-dimension variational data assimilation (4D-Var) approach was applied to estimate emissions using SO<sub>2</sub> data from OMI (Wang et al., 2016;Qu et al., 2019a), and NO<sub>2</sub> data from SCIAMACHY, GOME-2, and OMI (Kurokawa et al., 2009;Qu et al., 2017;Kong et al., 2019). The 4D-Var posterior has a smaller root mean square error than the mass balance posterior, especially in the conditions when the initial guess and true emissions have different spatial patterns (Qu et al., 2017); this is because the spatial extent of  
85 source influences on modelled column concentrations (Turner et al., 2012) are only indirectly [and partially](#) accounted for in the mass balance approach. Cooper et. al (2017), however, showed that the iterative finite difference mass balance approach has similar [normalized mean error value as the 4D-Var approach for global-scale models with coarse resolution when synthetic NO<sub>2</sub> columns observations are used to constrain NO<sub>x</sub> emissions](#). To combine the strengths of the 4D-Var and mass balance approaches, Qu et al. (2017) further  
90 introduced a hybrid 4D-Var-mass-balance approach, which can better capture trends and spatial variability of NO<sub>x</sub> emissions than the mass balance approach and save significant computational resources when applied to constrain monthly NO<sub>x</sub> emissions for multiple years. Other data assimilation approaches including the ensemble Kalman

filter method (Miyazaki et al., 2012;Miyazaki et al., 2017) and the Daily Emission estimates Constrained by Satellite Observation (DECISO) algorithm (Mijling and van der A, 2012;Ding et al., 2015) have also been used to  
95 constrain NO<sub>x</sub> emissions.

Here, we focus on the development and feasibility for joint 4D-var assimilation of satellite-based SO<sub>2</sub> and NO<sub>2</sub> data to optimize SO<sub>2</sub> and NO<sub>x</sub> emission strengths simultaneously. Specifically, this study aims to conduct 4D-Var assimilation of VCDs of SO<sub>2</sub> and NO<sub>2</sub> from OMPS to constrain SO<sub>2</sub> and NO<sub>x</sub> emissions over China using the  
100 GEOS-Chem 4D-Var inverse modeling framework. In our companion study (Wang et al., 2019), we develop approaches to downscaling the optimized emission inventories for improving air quality predictions. Despite their numerous applications for top-down estimate of SO<sub>2</sub> and NO<sub>x</sub> emissions in the past two decades, GOME and SCIAMCHY stopped providing data in 2004 and 2012, respectively, while OMI has been suffering from a row anomaly that leads to much less spatial coverage and larger data uncertainty (Schenkeveld et al., 2017). Hence, it  
105 is important to study the potential of next-generation sensors such as OMPS toward continuously monitoring the change of SO<sub>2</sub> and NO<sub>x</sub> emissions and their atmospheric loadings. Two OMPS sensors onboard Suomi NPP and NOAA-20 have been launched in 2011 and 2018, respectively, and the third one is expected to be launched in 2020. As OMPS will continue to provide SO<sub>2</sub> and NO<sub>2</sub> retrievals in the next two decades, this study, [for the first time](#), seeks to provide a critical assessment of the extent to which the OMPS observations improve emissions  
110 estimates and air quality forecast at the regional scale.

The novelty of this study lies not only in the first application of OMPS SO<sub>2</sub> and NO<sub>2</sub> retrievals to constrain emissions using the 4D-Var technique but also in the deployment of OMI data to assess the GEOS-Chem simulation with posterior emissions, thereby studying the degree to which OMPS and OMI retrievals, despite their  
115 difference in sensor characteristics and inversion techniques, can provide consistent constraints for the model improvement. Qu et al. (2019a) showed that posterior SO<sub>2</sub> emissions [derived](#) from different OMI SO<sub>2</sub> products vary in strength and have consistent trend signs. Our study here using OMPS thus [examines](#) an important issue, which is whether or not there would be any artificial trends in our climate data record of atmospheric SO<sub>2</sub> and NO<sub>2</sub> due to the transition of satellite sensors ([Wang and Wang, 2020](#)). Our study is also different from past studies  
120 (Wang et al., 2016;Qu et al., 2017;Qu et al., 2019a;Qu et al., 2019b) that have applied the 4D-Var technique to OMI data with the GEOS-Chem adjoint model, but did not include evaluation with independent satellite data. Qu et al. (2019b) showed joint inversion using OMI SO<sub>2</sub> and NO<sub>2</sub> benefits from simultaneous adjustment of OH and O<sub>3</sub> concentrations, which supports assimilating OMPS SO<sub>2</sub> and NO<sub>2</sub> observations simultaneously in this study.

125 Additionally, considering that the uncertainty of NH<sub>3</sub> emission inventories is up to 153% over China (Kurokawa  
et al., 2013) and NH<sub>3</sub> emissions are not constrained in our inversions, we also explore issues related to the co-  
variation among species that appear to be independent but indeed are connected through chemical processes and  
analyze the differences in responses of emissions and aerosols to NH<sub>3</sub> emissions uncertainty between joint and  
single-species assimilations. Finally, this paper also provides the foundation for the Part II investigation (Wang  
et al., 2019) in which we develop various downscaling methods to illustrate that optimized emission, albeit its  
130 coarse resolution inherent from OMPS data, can be used to improve the air quality forecast at the resolution much  
finer than OMPS pixel size.

We describe OMPS and OMI data in Sect. 2. The GEOS-Chem model and its adjoint as well as the design of  
numerical experiments are presented in Sect. 3. Results of case studies for October 2013 are provided in Sect. 4.  
135 Sect. 5 consists of discussion and conclusions.

## 2. Data

### 2.1 OMPS data as constraints

We use OMPS Level-2 SO<sub>2</sub> and NO<sub>2</sub> tropospheric VCDs in October 2013 as constraints to optimize SO<sub>2</sub> and NO<sub>x</sub>  
emissions over China. The OMPS nadir mapper on board the Suomi-NPP satellite, launched in November 2011,  
140 observes hyperspectral solar radiance and earthshine radiance at 300-380 nm (Flynn et al., 2014). With 35  
detectors of 50x50 km nominal pixel size in cross-track direction, OMPS has a swath of 2800 km flying across  
the equator at 1:30 PM local time ascendingly at the sunlit side of the Earth surface and providing global coverage  
daily. Both SO<sub>2</sub> and NO<sub>2</sub> are retrieved through the Direct Vertical Column Fitting (DVCF) algorithm with SO<sub>2</sub>  
and NO<sub>2</sub> atmospheric profile information from GEOS-Chem simulations and have a retrieval precision of 0.2 DU  
145 and 0.011 DU, respectively, which are estimated from the standard background (a clean region that is far from  
emission sources) retrievals (Yang et al., 2013; Yang et al., 2014). These precision values can be used as the  
observation error in the cost function of data assimilation. However, we should notice that the estimated  
observation (retrieval) errors only represent the observation error distribution of the products a whole; it cannot  
represent the observation error distribution for every pixel, because the pixel-level error is amenable to  
150 spatiotemporal change of cloud fraction, satellite observation geometry, aerosol impacts, etc. In theory, if the  
uncertainties can be analytically described at the pixel level, they would be directly applied to improve the satellite  
product in the first place.

Only pixels with both Solar Zenith Angle (SZA) and View Zenith Angle (VZA) less than 75° are used, as larger  
155 SZA or VZA result in longer light path length, and consequently less information content and lower data quality  
for retrieving the change of SO<sub>2</sub> or NO<sub>2</sub> loadings in the Plane Boundary Layer (PBL) where the two trace gases  
from anthropogenic sources mainly concentrate. We also remove the pixels with Radiative Cloud Fraction (RCF)  
larger than 0.2 for SO<sub>2</sub> and 0.3 for NO<sub>2</sub> as a trade-off between the data amount and cloud impacts. Considering  
their large uncertainty, OMPS SO<sub>2</sub> retrievals in the grid cell where the prior simulation is less than 0.1 DU will  
160 not be used, except in Quality Control (QC) sensitivity analysis experiments.

## 2.2 OMI data for assessment

OMI Level-3 SO<sub>2</sub> and NO<sub>2</sub> tropospheric VCDs at a spatial resolution of 0.25°x0.25° from NASA are used for  
evaluating the model results. OMI is a UV-vis hyperspectral sensor that observes solar irradiance and earthshine  
radiance at 300-500 nm. The swath of OMI is 2600 km, consisting of 60 detectors with the nominal pixel size of  
165 13x24 km<sup>2</sup> at nadir. OMI flies across the equator in the ascending node at 1:45 PM local time, which is very close  
to the 1:30 PM local time for OMPS. Due to row anomaly (Schenkeveld et al., 2017), OMI takes more than one  
day to provide global coverage. The Level-3 product is derived from the Level-2 product; the latter is retrieved  
through the Principal Component Analysis (PCA) algorithm with a fixed Air Mass Factor (AMF) assumption for  
SO<sub>2</sub> (Li et al., 2013) and variation of the Differential Optical Absorption Spectroscopy (DOAS) algorithm for  
170 NO<sub>2</sub> (Krotkov et al., 2017; Marchenko et al., 2015), with a precision of 0.5 DU (Li et al., 2013) and 0.017 DU  
(Krotkov et al., 2017), respectively. In the Level-3 product, pixels affected by row anomaly are removed. For SO<sub>2</sub>,  
only the pixel with the shortest light path, SZA less than 70°, RCF less than 0.2, and detector number in the range  
of 2 to 59 (1-based) is retained in a 0.25°x0.25° grid cell and then corrected with a new AMF based on GEOS-  
Chem SO<sub>2</sub> profile simulation (Leonard, 2017). For the OMI Level-2 NO<sub>2</sub> product, the AMF calculation is based  
175 on Global Modeling Initiative NO<sub>2</sub> profile simulation (Krotkov et al., 2017), and all pixels with SZA less than  
85°, terrain reflectivity less than 0.3, RCF less than 0.3 are averaged in a 0.25°x0.25° grid cell weighted by the  
overlapping area of grid cell and pixel to form Level-3 product (Bucsela et al., 2016). In the assessments, OMI  
observations are averaged at 2°x2.5° model grid cell, and model simulations are sampled by OMI observational  
time.

## 180 3. Method

### 3.1 GEOS-Chem and its adjoint

GEOS-Chem is a 3-D chemistry transport model driven by emissions and GEOS-FP meteorological fields. The secondary sulfate-nitrate-ammonium aerosol formation in the model is introduced by Park et al. (2004). Both aerosols and gases are removed by wet deposition, including washout and rainout from large-scale or convective precipitation (Liu et al., 2001) and the dry deposition following a resistance-in-series scheme with aerodynamic resistance and boundary resistance calculated from GEOS-FP meteorological field and surface resistances based largely on a canopy model (Wang et al., 1998; Wesely, 1989). Anthropogenic SO<sub>2</sub>, NO<sub>x</sub>, and NH<sub>3</sub> emissions used over East Asia are the mosaic emission inventory (MIX) (Li et al., 2017b) for year 2010. SO<sub>2</sub> and NO<sub>2</sub> VCDs are simulated at 2°x2.5° resolution with 47 vertical layers using both the prior and posterior emission inventories to compare with OMI retrievals.

The GEOS-Chem adjoint model is a tool for efficiently calculating the sensitivity of a scalar cost function with respect to large numbers of model parameters simultaneously such as emissions (Henze et al., 2007). In this study, the cost function is defined as Eq. (1).

$$J(\boldsymbol{\sigma}) = \gamma \frac{1}{2} [\mathbf{H}_{\text{SO}_2}(\mathbf{M}(\boldsymbol{\sigma})) - \mathbf{c}_{\text{SO}_2}]^T \mathbf{S}_{\text{SO}_2}^{-1} [\mathbf{H}_{\text{SO}_2}(\mathbf{M}(\boldsymbol{\sigma})) - \mathbf{c}_{\text{SO}_2}] + \frac{1}{2} [\mathbf{H}_{\text{NO}_2}(\mathbf{M}(\boldsymbol{\sigma})) - \mathbf{c}_{\text{NO}_2}]^T \mathbf{S}_{\text{NO}_2}^{-1} [\mathbf{H}_{\text{NO}_2}(\mathbf{M}(\boldsymbol{\sigma})) - \mathbf{c}_{\text{NO}_2}] + \frac{1}{2} [\boldsymbol{\sigma} - \boldsymbol{\sigma}_a]^T \mathbf{S}_a^{-1} [\boldsymbol{\sigma} - \boldsymbol{\sigma}_a] \quad (1)$$

$\mathbf{E}$  is a vector in which SO<sub>2</sub> and NO<sub>x</sub> emissions are ordered by GEOS-Chem model grid cell and by species.  $\mathbf{E}_a$  is a prior estimate, and  $\boldsymbol{\sigma}$  is a state vector, consisting of  $\ln(\mathbf{E}_i/\mathbf{E}_{a,i})$ , where  $\mathbf{E}_i$  and  $\mathbf{E}_{a,i}$  are the  $i$ th element in  $\mathbf{E}$  and  $\mathbf{E}_a$ , respectively.  $\mathbf{c}_{\text{SO}_2}$  and  $\mathbf{c}_{\text{NO}_2}$  are vectors of OMPS SO<sub>2</sub> and NO<sub>2</sub> tropospheric VCDs, respectively.  $\mathbf{S}_{\text{SO}_2}$  and  $\mathbf{S}_{\text{NO}_2}$  are observation error covariance matrixes for SO<sub>2</sub> and NO<sub>2</sub> and are assumed to be diagonal, which means observational errors are uncorrelated.  $\mathbf{M}$  is the GEOS-Chem model that simulates the relationship between SO<sub>2</sub> and NO<sub>2</sub> concentrations in the atmosphere and the emissions factors.  $\mathbf{H}_{\text{SO}_2}$  and  $\mathbf{H}_{\text{NO}_2}$  are observation operators which map GEOS-Chem simulations of SO<sub>2</sub> and NO<sub>2</sub> to the observational space, respectively.  $\boldsymbol{\sigma}_a$  is the prior estimate of  $\boldsymbol{\sigma}$ , and  $\mathbf{S}_a$  is the error covariance matrix for  $\boldsymbol{\sigma}_a$ .  $\mathbf{S}_a$  is assumed to be diagonal with a relative error of 50% for SO<sub>2</sub> and 100% for NO<sub>x</sub> as used in Xu et al. (2013).  $\gamma$  is a parameter we introduce to balance the importance of the SO<sub>2</sub> observation term (first term on the right side of Eq. (1)) and NO<sub>2</sub> observational term (second term on the right side of Eq. (1)), given both the different sizes and observation errors of these two observation datasets.

210

OMPS SO<sub>2</sub> and NO<sub>2</sub> tropospheric VCDs are directly compared to GEOS-Chem tropospheric VCDs of SO<sub>2</sub> ( $H_{\text{SO}_2}(\mathbf{M}(\boldsymbol{\sigma}))$  in Eq. (1)) and NO<sub>2</sub> ( $H_{\text{NO}_2}(\mathbf{M}(\boldsymbol{\sigma}))$  in Eq. (1)). Retrieving satellite SO<sub>2</sub> and NO<sub>2</sub> tropospheric VCDs requires assumptions regarding SO<sub>2</sub> and NO<sub>2</sub> vertical profiles, as the sensitivity of the radiance observed by satellite sensors to the changes of SO<sub>2</sub> or NO<sub>2</sub> loadings is a function of plume height. If the vertical profile assumptions in the retrieval process are inconsistent with the GEOS-Chem simulations, the inconsistency partly contributes to the difference between the GEOS-Chem simulations and the OMPS retrievals ( $H_{\text{SO}_2}(\mathbf{M}(\boldsymbol{\sigma})) - \mathbf{c}_{\text{SO}_2}$  or  $H_{\text{NO}_2}(\mathbf{M}(\boldsymbol{\sigma})) - \mathbf{c}_{\text{NO}_2}$ ). In this study, OMPS SO<sub>2</sub> and NO<sub>2</sub> tropospheric VCDs are retrieved using the shape of vertical profiles from GEOS-Chem simulations (Yang et al., 2013; Yang et al., 2014), but the differences of model version, simulation year, and emission inventory still exist. These differences still can lead to the differences of vertical profiles, hence partly contributing to the difference between the GEOS-Chem simulations and the OMPS retrievals. The vertical profile differences can lead to a mean bias of -6.8% overall at the pixel level (Fig. S1) and -7.5% (Fig. S2) for OMPS SO<sub>2</sub> and NO<sub>2</sub> retrievals, respectively. And we shall discuss the impacts of these bias on emission inverse modeling in Sect. 4.1.1.

225 In the optimization formulation, the forward model errors are also considered as part of the observation error term. However, while several ways to construct model error covariance matrix exist, including the Hollingworth-Lönnerberg (Hollingsworth & Lönnerberg, 1986) and NMC (Bannister, 2008) methods, their application for off-line CTM model error characterization deserves a separate a study. The Hollingsworth method extracts observation error variance (including forward model error) from (observation – background) covariance statistics with the assumptions that observation error is spatially uncorrelated, background error is spatially correlated as a function of distance, and observation error and background error are uncorrelated. The assumption that background error is spatially correlated as a function of distance only is suitable for the meteorological fields that vary smoothly, but for chemical species, emissions also contribute significantly to model errors and emissions are spatially correlated. The NMC method is normally applied to weather forecast models or on-line-coupled weather-chemistry models (Benedetti and Fisher, 2007). Off-line CTMs such as GEOS-Chem use the meteorological reanalysis and so, NMC is not applicable here to quantify the CTM’s transport error. Consequently, CTM’s transport errors are neglected in the past emission optimization work (Wang et al., 2016) and are adopted in this study. Admittedly, this simplification should be studied in future together with the evaluation and developments of methods to characterize off-line CTM errors.

240



We developed the observation operators for OMPS SO<sub>2</sub> and NO<sub>2</sub>, and the validations are shown in Fig. 1. The sensitivities of the cost function with respect to anthropogenic SO<sub>2</sub> and NO<sub>x</sub> emissions from the adjoint model is consistent with the sensitivities calculated through the finite difference approach. Hence, Fig. 1 confirms the correctness of the new observation operators integrated into the GEOS-Chem adjoint model.

245

To optimize the emission inventories,  $\sigma$  is adjusted iteratively until the cost function is minimized. The minimization is conducted with the L-BFGS-B algorithm (Byrd et al., 1995), which utilizes the sensitivity of the cost function with respect to  $\sigma$  that is calculated by the GEOS-Chem adjoint model. The minimization process halts when the difference in the cost function between two consecutive iterations is less than 3%. **This selection is to expediate the computation while still maintain the similar accuracy for the optimization; further tests show that the more iterations (after <3% reduction of cost function) doesn't yield discernable difference in the cost function values (Fig. S3) and optimization results (Table S1 and S2).**

250

### 3.2 Experiment design

Several elements play a role in the inverse modeling of emissions, including data quality control, balancing the spatial distributions of observational frequencies for the same species, balancing the observation contributions from different species, and uncertainties in the NH<sub>3</sub> emission inventory (because NH<sub>3</sub> has impacts on SO<sub>2</sub> and NO<sub>2</sub> lifetimes). To investigate the impacts of these factors on the posterior emissions, we design a set of experiments as summarized in Table 1 and Table 2. All these experiments use OMPS SO<sub>2</sub> and NO<sub>2</sub> retrievals to optimize corresponding emissions over China in October 2013 at a horizontal resolution of 2°×2.5°. Although finer resolution options such as 0.5°×0.625° or 0.25°×0.3125° are available for China, the 2°×2.5° resolution is selected for two reasons: (1) Save computational time; (2) chiefly, the coarse resolution of OMPS retrievals (50 km × 50 km at nadir and 190 km × 50 km at edges) has no first-order information to resolve the emissions at fine-resolution of 0.5°×0.625° or 0.25°×0.3125°. In Part II (Wang et al., 2019) of this study, we develop downscaling tools for regional air quality modeling. Indeed, one of the goals of the two-part investigation is to illustrate how OMPS data could be used to improve the air quality forecast at the resolution much finer than OMPS pixel size.

260

265

#### 3.2.1 Control experiments

The first control experiment is E-SO<sub>2</sub> (Table 1), in which only OMPS SO<sub>2</sub> tropospheric VCDs are used to constrain SO<sub>2</sub> emissions by removing the second additive term on the right side of Eq. (1). **Consequently,  $\gamma$  is set**

to unity. If the OMPS SO<sub>2</sub> tropospheric VCD error is set to 0.2 DU (Yang et al., 2013) for every pixel, the SO<sub>2</sub> observational term in the cost function (first term on the right side of Eq. (1)) over the North China Plain is much larger than that over Southwestern China (Fig. 2b), which yield high possibility to over-constrain the former and under-constrain the latter. The spatially unbalanced cost function is caused by cloud screening, as the number of observations over Southwestern China is much less than that over the North China Plain (Fig. 2a). To balance the cost function by accounting for this difference in the number of observations, SO<sub>2</sub> observation error is set to 0.2 DU multiplied by the square root of the number of OMPS overpasses that have SO<sub>2</sub> observation in the 2°x2.5° GEOS-Chem grid cell. The balance approach essentially normalizes observation terms in the cost function by the observation counts, which has been used in our study (Xu et al., 2015) to optimally invert aerosol optical properties from the skylight polarization and intensity measurements by AEROSOL ROBOTIC NETWORK (AERONET).

In the second experiment, E-NO<sub>2</sub>, OMPS NO<sub>2</sub> tropospheric VCDs alone are used to constrain NO<sub>x</sub> emissions by removing the first additive term on the right side of Eq. (1). Due to cloud screening, much more OMPS NO<sub>2</sub> observations exist over the North China Plain than over Southwestern China, which also could lead to a spatially unbalanced cost function if the OMPS NO<sub>2</sub> observation error is uniform. The OMPS NO<sub>2</sub> observation error is, however, assumed to be 0.011 DU (Yang et al., 2014) for every pixel in this study, regardless of location, because the NO<sub>x</sub> emissions adjustments during the inverse modeling process are supposed to be mainly over the North China Plain where prior NO<sub>x</sub> emissions are much larger than those over Southwestern China. In this study, we optimize emission scale factors rather than the emissions themselves. As a result, emissions are adjusted mainly at locations where prior emissions are large and kept as zero for those (2°x2.5°) grid boxes of zero prior emissions.

In the third experiment, E-joint, both the SO<sub>2</sub> and NO<sub>2</sub> from OMPS are used simultaneously for two reasons. Firstly, SO<sub>2</sub> and NO<sub>2</sub> concentrations can affect each other through several pathways. For example, Qu et. al (2019b) showed that the change of SO<sub>2</sub> or NO<sub>x</sub> emissions lead to the changes of O<sub>3</sub> and OH concentrations, hence the changes of SO<sub>2</sub> and NO<sub>2</sub> oxidations. Here, we will explore how the optimization results may dependent on the uncertainty of ammonia emissions (as elaborated in Sect. 3.2.2). Secondly, the computational time is reduced by ~50% in the joint assimilation as compared to separate assimilations when computational resource are restricted to running individual inversions sequentially (as opposed to in parallel), and energy usage is also saved; the latter require the realization of GEOS-chem adjoint twice, while only once is needed by the former.

In the E-joint experiment, observational terms for SO<sub>2</sub> and NO<sub>2</sub> in the cost function should be balanced through setting  $\gamma$  in Eq. (1). When it is not balanced, SO<sub>2</sub> observations have very little impact on the inversion results as the optimization algorithm will firstly minimize the observational term for NO<sub>2</sub> unless many more iterations than is computationally feasible are performed, which is caused by the fact that observational error and valid number of NO<sub>2</sub> observation are respectively smaller and larger than the counterparts of SO<sub>2</sub>. We thus subjectively derive  $\gamma$  in a non-arbitrary way in order to focus equally on both species, thereby tackling the imbalance in their observational constraints. In this manner, the cost function is defined to server the purpose of joint inversion of SO<sub>2</sub> and NO<sub>2</sub> emissions. Initially, we set  $\gamma$  to be the ratio of number of NO<sub>2</sub> observations to the number of SO<sub>2</sub> observations. This approach is not feasible here as the SO<sub>2</sub> observational error in E-SO<sub>2</sub> is much larger than the NO<sub>2</sub> observational error in E-NO<sub>2</sub>; not only does the number of observations play a role, but the observation error also has important impacts on balancing the cost function. If  $\gamma$  is simply set as unity, the NO<sub>2</sub> observational term in Eq. (1) is a factor of ~200 larger than the SO<sub>2</sub> observational term, which can lead to OMPS SO<sub>2</sub> in the E-joint experiment to be negligible. Consequently, to balance the two terms,  $\gamma$  is set as 200 (ratio of observational term in E-NO<sub>2</sub> to that in E-SO<sub>2</sub>) in E-joint and sensitivity experiments of using different values of  $\gamma$  are conducted (see section 3.2.2). Similar balance approach that adjusts contribution of observation terms in the cost function is used in the past work that assimilates satellite trace gas retrievals to invert emissions (Qu et al., 2019b) or invert the aerosol optical properties from skylight polarization measurements of AERONET (Xu et al., 2015).

### 3.2.2 Sensitivity experiments

To investigate the impacts of data quality control and spatially balancing the cost function on optimizing SO<sub>2</sub> emissions only, we design two sensitivity experiments. The first is E-SO<sub>2</sub>-noQC-noBL that is similar to E-SO<sub>2</sub> except that: (1) OMPS SO<sub>2</sub> retrievals in the 2°x2.5° grid cell where the prior GEOS-Chem simulation is less than 0.1 DU are also assimilated, i.e. without QC; (2) OMPS SO<sub>2</sub> observation error is set as 0.2 DU for every pixel, which means we do not spatially balance the cost function. The second sensitivity experiment is E-SO<sub>2</sub>-noBL in which the cost function is not spatially balanced, and it uses the same setting as E-SO<sub>2</sub> except for assuming an observation error of 0.2 DU uniformly.

To evaluate the effect of  $\gamma$  (of 200) in E-joint, we further test  $\gamma$  values of 20, 50, 100, 300, 500, 1000, 1500, and 2000 in the joint inversions; hereafter these experiments are named E-joint-d $\gamma$ . Through these sensitivity experiments, we study the proper  $\gamma$  range for jointly assimilating OMPS SO<sub>2</sub> and NO<sub>2</sub>. In future studies that may be conducted to jointly assimilate OMPS SO<sub>2</sub> and NO<sub>2</sub> for other months to obtain a long-term optimized emission

inventory, it is proposed to set proper  $\gamma$  values for each month based on the range with easy adjustment according  
 330 to the numbers of OMPS SO<sub>2</sub> and NO<sub>2</sub> observations and their associated errors.

NH<sub>3</sub> emissions are not optimized in our inverse modeling and yet their uncertainty is up to 153% over China  
 (Kurokawa et al., 2013). Thus, it is important to evaluate how this uncertainty may affect posterior SO<sub>2</sub> and NO<sub>x</sub>  
 emissions. Wang et al. (2013) emphasized the importance of controlling NH<sub>3</sub> to alleviate PM<sub>2.5</sub> pollution over  
 335 China, however it could worsen acid rain (Liu et al., 2019). Changes of NH<sub>3</sub> emissions is expected to change  
 ammonium and nitrate aerosol concentrations, or the aerosol surface area for heterogeneous N<sub>2</sub>O<sub>5</sub> chemistry,  
 hence affecting NO<sub>2</sub> concentrations or posterior NO<sub>x</sub> emissions in the inverse modeling. The change of posterior  
 NO<sub>x</sub> emissions is expected to lead to the change of posterior SO<sub>2</sub> emissions in the joint inverse modeling. Thus,  
 we shall investigate if NH<sub>3</sub> emissions are reduced to 50% and 20%, how the optimized SO<sub>2</sub> and NO<sub>2</sub> emission  
 340 inventories would change. Correspondingly, all these experiments are summarized in Table 2. E-SO<sub>2</sub>-0.5NH<sub>3</sub>, E-  
 NO<sub>2</sub>-0.5NH<sub>3</sub>, and E-joint-0.5NH<sub>3</sub>- $\gamma$ 500 in Table 2 are similar to E-SO<sub>2</sub>, E-NO<sub>2</sub>, and E-joint- $d\gamma$  ( $\gamma=500$ ) in Table  
 1, respectively, but NH<sub>3</sub> emissions are set to 50% of the original values. Similarly, E-SO<sub>2</sub>-0.2NH<sub>3</sub>, E-NO<sub>2</sub>-0.2NH<sub>3</sub>,  
 and E-joint-0.2NH<sub>3</sub>-  $\gamma$ 500 are the scenarios that NH<sub>3</sub> emissions are set to 20% of the original values.

### 3.3 Evaluation statistics

We use linear correlation coefficient (R), root mean square error (RMSE), mean bias (MB), normalized mean bias  
 (NMB), normalized standard deviation (NSD), and normalized centered root mean square error (NCRMSE) as  
 measures to evaluate GEOS-Chem SO<sub>2</sub> and NO<sub>2</sub> VCD simulations with satellite (OMPS and OMI) observations.  
 NSD is the ratio of the standard deviation of the simulation to the standard deviation of the observation. NCRMSE  
 is similar to RMSE, but the impact of bias is removed. This is shown in Eq. (2), where  $i$  is the  $i$ <sup>th</sup> grid cell,  $N$  is  
 350 the total number of grid cells,  $M_i$  and  $O_i$  are the  $i$ <sup>th</sup> GEOS-Chem simulation and satellite observation, respectively,  
 and  $\bar{M}$  and  $\bar{O}$  are averages of GEOS-Chem simulation and satellite observation, respectively. A composite  
 summary of these statistics is provided by the Taylor diagram (Taylor, 2001) which is a quadrant which  
 summarizes R (shown as cosine of polar angle), NSD (shown as radius from the quadrant center), and NCRMSE  
 (shown as radius from expected, satellite observation, point, which is located at the point where R and NSD are  
 355 unity).

$$\text{NCRMSE} = \frac{\sqrt{\frac{1}{N} \sum_{i=1}^N [(M_i - \bar{M}) - (O_i - \bar{O})]^2}}{\sqrt{\frac{1}{N} \sum_{i=1}^N (O_i - \bar{O})^2}} \quad (2)$$

## 4. Results

### 4.1 Separate and joint assimilations of SO<sub>2</sub> and NO<sub>2</sub>

#### 4.1.1 Self-consistency check

360 The cost functions are reduced by 41.6%, 27.6%, and 28.6% for E-SO<sub>2</sub>, E-NO<sub>2</sub>, and E-joint, respectively, and the results are shown in Fig. 3. Noticeably, hot spots of SO<sub>2</sub> VCDs over the North China Plain and the Sichuan Basin are shown in the OMPS observations (Fig. 3a), prior (Fig. 3b), posterior E-SO<sub>2</sub> (Fig. 3c), and posterior E-joint (Fig. 3d) simulations, however the prior simulation has an NMB of 106.5% (Fig. 3i) when compared with OMPS. The SO<sub>2</sub> NMB (106.5%) between GOES-Chem prior simulation and OMPS is much larger than the NMB (-6.8%,  
365 Fig S1) caused by the difference of SO<sub>2</sub> vertical profiles between OMPS SO<sub>2</sub> retrieval algorithm and current prior simulation; thus averaging kernel is not considered in the OMPS SO<sub>2</sub> observation operator. This large positive NMB decreases to 13.0% and 38.3% in the posterior E-SO<sub>2</sub> (Fig. 3j) and E-joint (Fig. 3k) simulations with an RMSE decreasing from 0.42 DU to 0.13 DU and 0.20 DU and R increasing from 0.62 to 0.72 and 0.64, respectively. Large NO<sub>2</sub> values are found over the North China Plain and Eastern China with large NO<sub>x</sub> emissions  
370 from the transportation sector (Fig. 3e-h). Comparing with OMPS NO<sub>2</sub>, GEOS-Chem results have an RMSE of 0.05 DU in the prior simulation (Fig. 3l) and reduce to 0.02 DU and 0.03 DU for E-NO<sub>2</sub> (Fig. 3m) and E-joint (Fig. 3n), with R increasing from 0.95 to 0.99 and 0.98, respectively.

Similarly, the averaging kernel is not considered in the OMPS NO<sub>2</sub> observation operator for optimization for the  
375 following reasons. First, the OMPS NO<sub>2</sub> retrieval differences due to the profile differences can lead to a NMB of -7.5% (Fig S2), which is still smaller than the prior GEOS-Chem simulation NMB (10.9%, Fig. 3l). Second, a NMB of 10.9% for model NO<sub>2</sub> VCD simulation is not a very large value, as the difference between satellite NO<sub>2</sub> VCD retrievals and ground-based measurements could be comparable to this value. For example, Krotkov et al. (2017) shows that OMI NO<sub>2</sub> VCD retrievals, on average, are ~10% larger than ground-based FTIR spectrometer.  
380 Thus, current research should mainly focus on the change of the spatial distribution (such as linear correlation coefficient) rather than bias of prior and posterior GEOS-Chem NO<sub>2</sub> VCD simulation. Finally, given that linear correlation coefficient between OMPS retrievals and that are modified through integration of averaging kernel and NO<sub>2</sub> vertical profile from this study is as large as 0.99, averaging kernel is not treated in the OMPS NO<sub>2</sub> observation operator. In general, the E-SO<sub>2</sub> and E-NO<sub>2</sub> posterior simulations show better results than E-joint,  
385 which may be affected by the value of  $\gamma$ , which we will discuss in Sect. 4.3.

### 4.1.2 Emissions

The anthropogenic SO<sub>2</sub> and NO<sub>x</sub> prior MIX emissions for October 2010 and posterior emissions from E-SO<sub>2</sub>, E-NO<sub>2</sub>, and E-joint for October 2013 are shown in Fig. 4. SO<sub>2</sub> and NO<sub>x</sub> hot spots are found in the prior emissions over both the North China Plain and Eastern China, while large SO<sub>2</sub> emissions are also at Southwestern China.

390 Anthropogenic SO<sub>2</sub> emissions over China are 1166 Gg S in prior MIX for October 2010 (Fig. 4a), dropping 418 Gg S (Fig. 4b) and 306 Gg S (Fig. 4c), or 35.8% and 26.2%, in E-SO<sub>2</sub> and E-joint, respectively, for October 2013. The differences between the estimates of this study and the MIX emission inventory, however, should not be considered as trends, and they are derived from different approaches. Posterior E-joint total anthropogenic SO<sub>2</sub> emissions are 112 Gg, or 15% larger than E-SO<sub>2</sub> over China (Fig. 4e). Regionally, positive differences between E-joint and E-SO<sub>2</sub> anthropogenic SO<sub>2</sub> emissions are over most areas of Central China and Eastern China, and relative difference is up to 100% over Shanxi province. (Fig. 4f). Grids with large differences are generally in locations where prior anthropogenic SO<sub>2</sub> emissions are larger, which means the pattern is affected by the fact the algorithm optimize emission scale factors rather than emissions directly. Anthropogenic NO<sub>x</sub> emissions over China are reduced by 5.8% and 6.5% , from 714 Gg N in prior MIX for October 2010 (Fig 4g) to 672 Gg N (Fig. 400 4h) in E-NO<sub>2</sub> and 667 Gg N (Fig. 4i) in E-joint for October 2013. Although the relative difference between E-joint and E-NO<sub>2</sub> proved to be less than 2% in terms of total anthropogenic NO<sub>x</sub> emissions over China (Fig. 4k), it is up to 40% over Shanxi province, and both grids with large positive differences and grids with large negative differences exist over North China Plain (Fig. 4 l).

### 4.1.3 Independent evaluation with OMI data

405 The optimized emission inventories are evaluated by comparing prior and posterior GEOS-Chem simulations of SO<sub>2</sub> and NO<sub>2</sub> with OMI VCDs as shown in Fig. 5. We only focus on regions covered by OMPS observations, although smaller changes of emissions exist in outskirts regions where OMPS observations are not used. High SO<sub>2</sub> levels are shown over the North China Plain and the Sichuan Basin in both the prior and posterior simulations while OMI only observes hot spots over the former region (Fig. 5a-d). When validating with OMI SO<sub>2</sub> VCDs, the NMB is ~300% in the prior simulation, and it reduces to ~100% in E-SO<sub>2</sub> and ~130% in E-joint (Fig. 5i). Not only is the NMB reduced, but the spatial distributions are also improved with the NCRMSE reducing from ~1.6 in the prior simulation to ~0.7 in E-SO<sub>2</sub> and ~0.8 in E-joint, which is much closer to ~0.6 when comparing OMPS observations with OMI observations (Fig. 5i). For NO<sub>2</sub>, OMI observations and the prior and posterior simulations show large NO<sub>2</sub> concentrations over the North China Plain and Eastern China (Fig. 5e-h). The improvements for

415 E-NO<sub>2</sub> and E-joint are reflected in terms of R when evaluating with OMI tropospheric VCDs, although the two  
experiments show larger negative NMB than the prior simulation (Fig. 5j). In all the evaluations, OMI SO<sub>2</sub> and  
NO<sub>2</sub> VCD retrievals are not corrected by calculating new air mass factors that are derived from integrating  
scattering weights and corresponding vertical profiles of GEOS-Chem simulations of this study. However, Fig.  
S4 shows similar improvements if new air mass factors are applied, although statistic metric values are slightly  
420 different.

Here, OMPS observations and GEOS-Chem simulations are compared with OMI observations as an evaluation  
of posterior emission inventories, but it is not assumed that OMI provides the true status of SO<sub>2</sub> and NO<sub>2</sub> in the  
atmosphere. OMI and OMPS observe the same trend direction of SO<sub>2</sub> (NO<sub>2</sub>) over China, but the strengths of trend  
425 are quite different (Wang and Wang, 2020). OMPS SO<sub>2</sub> average is ~0.14 DU, or ~95% larger than OMI SO<sub>2</sub>, and  
the R of the two products is 0.81 (Fig. 6b). Thus, it is reasonable that posterior SO<sub>2</sub> is larger than OMI observations  
by ~100% in E-SO<sub>2</sub> and ~130% in E-joint. OMPS NO<sub>2</sub> is ~24% smaller than OMI (Fig. 6d), which explains why  
the posterior NO<sub>2</sub> simulations have larger negative NMB than the prior simulation when compared with the OMI  
observations. Our analysis also shows that the systematic difference among various satellite products for the same  
430 species (such as SO<sub>2</sub> or NO<sub>2</sub>) can lead to biases in constraining emissions, but the posterior GEOS-Chem  
simulations still show in terms of the spatial distribution of SO<sub>2</sub> and NO<sub>2</sub>.

#### 4.2 The impacts of QC and spatial balance

The results of E-SO<sub>2</sub>-noQC-noBL and E-SO<sub>2</sub>-noBL are compared with E-SO<sub>2</sub> to show the impacts of QC and  
spatial balance. Both OMPS retrievals and the GEOS-Chem prior simulations show that SO<sub>2</sub> VCDs over Inner  
435 Mongolia and the Sichuan Basin (grid cells M and S, respectively in Fig. 7) are smaller than those over the North  
China Plain; this pattern reverses in the posterior E-SO<sub>2</sub>-noQC-noBL simulation where SO<sub>2</sub> over the North China  
Plain becomes smaller than that over grid cells M and S. Grid cell M becomes more reasonable after conducting  
the data quality control by removing OMPS SO<sub>2</sub> in any grid cells where prior GEOS-Chem SO<sub>2</sub> VCDs are less  
than 0.1 DU (e.g., as in E-SO<sub>2</sub>-noBL, as shown in Fig. 7d). QC helps to improve models over grid cell M, as the  
440 data removed are close to Inner Mongolia, and are generally less than 0.1 DU, which are comparable to the  
retrieval error. SO<sub>2</sub> over grid cell S from E-SO<sub>2</sub>-noBL (Fig. 7d) is, however, still larger than that over the North  
China Plain, compared with the better spatial pattern from E-SO<sub>2</sub> (Fig. 3c). Thus, QC and spatial balancing of the  
cost function together improve the spatial pattern of the posterior GEOS-Chem SO<sub>2</sub> VCD simulation.

### 4.3 The impacts of $\gamma$ on joint assimilations

445 In addition to setting  $\gamma$  as 200 in E-joint, we test the impacts of using various  $\gamma$  values on joint assimilation in E-joint-d $\gamma$  for October 2013. All the SO<sub>2</sub> and NO<sub>2</sub> VCDs from prior and posterior E-joint and E-joint-d $\gamma$  simulations are compared with OMPS counterparts (Fig. 8a-b). Regardless of the  $\gamma$  values used, all the posterior simulations of SO<sub>2</sub> show smaller NMB and NCRMSE than the prior simulation when validating against OMPS and OMI counterparts, but the extents of improvement vary. When  $\gamma$  is 20, 50, or 100, the SO<sub>2</sub> terms are obviously under-  
450 constrained, and GEOS-Chem SO<sub>2</sub> NCRMSE, evaluated with OMPS observations, changes from ~1.8 in the prior simulation to in the range of ~1.4 to ~1.7 in the posterior E-joint-d $\gamma$  simulations, which are much larger than ~0.7 in E-SO<sub>2</sub> (Fig. 8a). Similarly, when  $\gamma$  is no larger than 100, the bias of GEOS-Chem SO<sub>2</sub>, validated with OMPS observations, only reduces from ~100% to ~75%, compared to ~25% in E-SO<sub>2</sub> (Fig. 8a), and the posterior SO<sub>2</sub> emissions are in the range of 1055 Gg S to 1143 Gg S, which are much larger than 748 Gg S from E-SO<sub>2</sub> (Table  
455 3). When  $\gamma$  is in the range of 200 to 2000, the SO<sub>2</sub> simulation results and emissions from joint assimilations are more similar to that from E-SO<sub>2</sub> than that with  $\gamma$  no larger than 100 (Fig. 8a and Table 3). Similar to SO<sub>2</sub>, the GEOS-Chem simulations of NO<sub>2</sub> in the sensitivity experiments improve in terms of R and NCRMSE in all joint assimilation tests, but the significance of  $\gamma$  is less than that for SO<sub>2</sub>. NO<sub>2</sub> NCRMSE is ~0.4 in the prior simulation when evaluating with OMPS counterparts, compared to the range of ~0.2 to ~0.25 in E-joint, E-joint-d $\gamma$  and E-  
460 NO<sub>2</sub> (Fig. 8b). The posterior NO<sub>x</sub> emissions are in the range of 662 Gg N to 682 Gg N, compared with 672 Gg N in E-NO<sub>2</sub> (Table 3).

The impacts of  $\gamma$  are also reflected when evaluating SO<sub>2</sub> and NO<sub>2</sub> simulations with OMI retrievals (Fig. 8c-d). Small  $\gamma$  values of 20, 50, and 100 lead to a much larger bias and NCRMES for SO<sub>2</sub> from E-joint-d $\gamma$  than that from  
465 E-SO<sub>2</sub>. For NO<sub>2</sub>, these small  $\gamma$  values make results from E-joint-d $\gamma$  very similar to that from E-NO<sub>2</sub>.

Considering all of the above analyses, the results with  $\gamma$  in the range of 200 to 2000 are deemed acceptable. The E-joint-d $\gamma$  ( $200 \leq \gamma \leq 2000$ ) emissions are within -3% to 15% of E-SO<sub>2</sub> for SO<sub>2</sub> and  $\pm 2\%$  of E-NO<sub>2</sub> for NO<sub>x</sub> in terms of total anthropogenic SO<sub>2</sub> and NO<sub>x</sub> emissions over China. When evaluating with OMPS observations, the  
470 NCRMSE of using the posterior emissions from the separate and joint ( $200 \leq \gamma \leq 2000$ ) inversions are ~60% and ~45%-60% smaller than that of using the prior emissions for SO<sub>2</sub>, respectively, and ~50% and ~38%-50% smaller than that of using the prior emissions for NO<sub>2</sub>, respectively.



When evaluating with OMI retrievals, joint inversion shows better results than separate inversion for SO<sub>2</sub> or NO<sub>2</sub>, but not both, depending on the value of  $\gamma$ . When  $\gamma$  is 20, 50, or 100, NO<sub>2</sub> NCRSME for E-joint-dy improvement appears to be smaller than that for E-NO<sub>2</sub>, but SO<sub>2</sub> NCRSME for E-joint-dy is larger than that for E-SO<sub>2</sub>. Conversely, when  $\gamma$  is 1000, 1500, or 2000, SO<sub>2</sub> NCRSME for E-joint-dy is smaller than that for E-SO<sub>2</sub>, but NO<sub>2</sub> NCRSME for E-joint-dy is larger than that for E-NO<sub>2</sub>. This is similar to the findings by Qu et al., (2019b) in which the months when joint inversion shows better result than separate inversion for SO<sub>2</sub> (NO<sub>2</sub>) have worse result for NO<sub>2</sub> (SO<sub>2</sub>). The benefit of joint inversion for improving only one species is similar to Qu et al. (2019b) and is likely to due to the complicated relationship between these two species through different chemical pathways. For example, O<sub>3</sub> and OH are key species that connect the chemistry of SO<sub>2</sub> and NO<sub>2</sub> and aerosols can affect the photolysis and heterogenous chemistry. Hence, while joint inversion to improve both species cannot be demonstrated here, it should be reviewed as the first step of simultaneously assimilating multiple species (including AOD, NH<sub>3</sub>, and other trace gases) to optimize emissions. Until then, the system is not ready to holistically evaluate the benefits of joint assimilation to improve the model in a systematic manner. It is worthy noting that Xu et al. (2013) showed the feasibility of using MODIS cloud-free radiance to optimize emissions of SO<sub>2</sub> and NO<sub>2</sub> at the same time. Future research should add the aerosol optical depth or visible reflectance (as well as tropospheric O<sub>3</sub> if reliable) as constraints to further evaluate the benefits of joint assimilation for improving model overall performance in a systematic matter.

#### 4.4 The impacts of NH<sub>3</sub> emission

In the single-species inversions, NH<sub>3</sub> emission uncertainty has weaker impacts on posterior SO<sub>2</sub> emissions than NO<sub>x</sub> emissions. Posterior SO<sub>2</sub> emissions over China are 748 Gg S in the 100% NH<sub>3</sub> emission scenario (E-SO<sub>2</sub>), and they only slightly reduce to 747 Gg S and 745 Gg S when NH<sub>3</sub> emissions are 50% (E-SO<sub>2</sub>-0.5NH<sub>3</sub>) and 20% (E-SO<sub>2</sub>-0.2NH<sub>3</sub>) of the original values, respectively (Table 4). The largest relative changes at model-grid-cell scale are only -2.5% (Fig. 9a) for E-SO<sub>2</sub>-0.5NH<sub>3</sub> for and -4.7% (Fig. 9b) for E-SO<sub>2</sub>-0.2NH<sub>3</sub>. All these results can be explained by considering how changes of NH<sub>3</sub> can potentially impact the lifetimes of SO<sub>2</sub> and NO<sub>2</sub> and hence affect SO<sub>2</sub> and NO<sub>2</sub> VCD simulations. When the NH<sub>3</sub> emissions decrease to 50%, and 20% SO<sub>2</sub> VCDs only increase up to 3.8% and 6.1%, respectively, in some grid cells over the Sichuan Basin in the prior simulations, and these changes are even much smaller over the North China Plain (Fig. 10a-b), as NH<sub>3</sub> has no direct effect on the life cycle of SO<sub>2</sub>. This is understandable because in GEOS-Chem, once SO<sub>2</sub> is oxidized to H<sub>2</sub>SO<sub>4</sub>, SO<sub>4</sub> remains as particulate sulfate regardless it is neutralized by NH<sub>3</sub> or not (Wang et al., 2008). Hence, the reductions

of NH<sub>3</sub> to 50% and 20% overall has minimal (negligible) impact on SO<sub>2</sub> amount in the prior simulation and the posterior separate SO<sub>2</sub> emission inversion.

505

Although the posterior NO<sub>x</sub> emissions in the scenarios of 50% (E-NO<sub>2</sub>-0.5NH<sub>3</sub>) and 20% (E-NO<sub>2</sub>-0.2NH<sub>3</sub>) NH<sub>3</sub> emission experiments of the original values are 5 Gg N (0.7%) and 19 Gg N (2.8%), respectively, which are smaller than those when using the original (E-NO<sub>2</sub>) NH<sub>3</sub> emissions over China (Table 4), the reduction is up to -4.0% (Fig. 9e) for E-NO<sub>2</sub>-0.5NH<sub>3</sub> and -9.1% (Fig. 9f) for E-NO<sub>2</sub>-0.2NH<sub>3</sub> in individual grid cells. These decreases are understood by simultaneous reduction of nitrate by 59.5% (Fig. 12h vs. 12g) and 80.5% (Fig 12i vs. 12g) and ammonium by 39.6% (Fig. 12n vs. 12m) and 67.5% (Fig. 12o vs. 12m), which leads to large reduction of the hydrated aerosol surface area for heterogeneous N<sub>2</sub>O<sub>5</sub> chemistry at night, hence overall NO<sub>2</sub> lifetime (Fig. 10c-d). N<sub>2</sub>O<sub>5</sub> normally forms at night by reaction between NO<sub>2</sub> and NO<sub>3</sub>, and thermally decomposes back to NO<sub>2</sub> and NO<sub>3</sub> (Seinfeld and Pandis, 2016), and hence the amount of N<sub>2</sub>O<sub>5</sub>, NO<sub>2</sub>, and NO<sub>3</sub> are in equilibrium through the reversible reaction. Since the hydrolysis of N<sub>2</sub>O<sub>5</sub> to form HNO<sub>3</sub> mainly occurs on hydrated aerosol particles (Seinfeld and Pandis, 2016), the decrease of hydrated aerosol surface area (due to reduction of NH<sub>3</sub> emission) leads to less hydrolysis of N<sub>2</sub>O<sub>5</sub> (an important sink for atmospheric NO<sub>x</sub>) and subsequently more NO<sub>2</sub> to be in the equilibrium with N<sub>2</sub>O<sub>5</sub> at night. As a result, the reduction of NH<sub>3</sub> emissions further increases the positive bias in the prior NO<sub>2</sub> simulations when comparing with OMPS observations, and to compensate such large positive bias, non-negligible decreases in the posterior NO<sub>x</sub> emissions are required (Fig. 9 e and f). The reduction of nitrate and ammonium aerosols can also increase sunlight reaching troposphere, hence photolysis O<sub>3</sub> and NO<sub>2</sub>. Figure S5 separates the impacts of increase of photolysis O<sub>3</sub> and NO<sub>2</sub> and decrease heterogeneous N<sub>2</sub>O<sub>5</sub> chemistry on NO<sub>2</sub> lifetime and shows that the former is negligible compared with the latter.

525 The decreases of posterior SO<sub>2</sub> and NO<sub>x</sub> emissions in the joint inversions caused by the reduction of NH<sub>3</sub> emissions are stronger than that in the separate inversions (Table 4 and Fig. 9). Although the changes of NH<sub>3</sub> emissions only have slight impacts on the SO<sub>2</sub> separate inversions (E-SO<sub>2</sub>, E-SO<sub>2</sub>-0.5NH<sub>3</sub>, and E-SO<sub>2</sub>-0.2NH<sub>3</sub>), the posterior SO<sub>2</sub> emission is 802 Gg S in E-joint-d $\gamma$  ( $\gamma=500$ ), down to 783 Gg S (decreasing by 2.4%) and 746 Gg S (decreasing by 7.0%) in E-joint-0.5NH<sub>3</sub>-  $\gamma 500$  and E-joint-0.2NH<sub>3</sub>-  $\gamma 500$ , respectively (Table 4); in some grid cells, the relative reductions are up to -9.0% (Fig. 9c) for E-joint-0.5NH<sub>3</sub>-  $\gamma 500$  and -27.7% (Fig. 9d) for E-joint-0.2NH<sub>3</sub>-  $\gamma 500$ . For posterior NO<sub>x</sub> emissions at the grid cells, the relative changes are up -15.2% (Fig. 9g) for E-joint-0.5NH<sub>3</sub>-  $\gamma 500$  and -29.4% (Fig. 9h) for E-joint-0.2NH<sub>3</sub>-  $\gamma 500$  with respect to E-joint-d $\gamma$  ( $\gamma=500$ ).

530

#### 4.5 Aerosol responses to emission changes

Although SO<sub>2</sub> emissions over the North China Plain (E-joint-d $\gamma$  ( $\gamma=500$ )) have decreased by more than 50%, and  
535 NO<sub>x</sub> emissions have also been reduced, reductions of Sulfate-Nitrate-Ammonium (SNA) Aerosol Optical Depth  
(AOD) over the same region are only up to 10% (Fig. 11). This is because the North China Plain is mainly polluted  
by nitrate rather than sulfate (Fig. 12a-l), and the reduction of SO<sub>2</sub> emissions will increase nitrate loadings in the  
atmosphere (Fig. 12g-l), which is also consistent with Kharol et al. (2013)'s research that shows nitrate  
concentrations decrease as SO<sub>2</sub> emissions increase; the reduction of SO<sub>2</sub> emissions lead to less H<sub>2</sub>SO<sub>4</sub> to react  
540 with NH<sub>3</sub>, which further favor the reaction of HNO<sub>3</sub> and NH<sub>3</sub> to form nitrate. As NH<sub>3</sub> emissions change reduce  
by 50% and 80% ammonium column loadings decrease by ~40% and ~70% (Fig. 12g-l), respectively, and nitrate  
column loadings decrease even by ~70% and ~90%, respectively (Fig. 12m-r).

#### 5. Discussion and conclusions

We developed 4D-var observation operators for assimilating OMPS SO<sub>2</sub> and NO<sub>2</sub> VCDs to constrain SO<sub>2</sub> and  
545 NO<sub>x</sub> emissions through GEOS-Chem adjoint model. The approach is applied for case study over China for  
October 2013 at 2°x2.5° resolution and the MIX 2010 is used as the prior emission inventory. Several experiments  
of assimilating OMPS SO<sub>2</sub> and NO<sub>2</sub> separately and jointly are conducted, and SO<sub>2</sub> and NO<sub>2</sub> VCDs from the  
GEOS-Chem prior and posterior simulations are compared with counterparts from OMPS and OMI.

550 OMPS SO<sub>2</sub> and NO<sub>2</sub> retrievals are separately and jointly used to constrain their corresponding emissions. In the  
single-species inversions, posterior anthropogenic SO<sub>2</sub> and NO<sub>x</sub> emissions are 748 Gg S and 672 Gg N for October  
2013, down from 1166 Gg S and 714 Gg N in the prior MIX for October 2010, respectively. In the joint inversions  
of assimilating OMPS SO<sub>2</sub> and NO<sub>2</sub> simultaneously, the cost function is balanced according to the values of  
observational terms rather than the number of observations. When the cost function is well balanced ( $\gamma$  in the  
555 range of 200 to 2000), the results of the joint inversions are within -3% to 15% of the single-species inversion for  
total anthropogenic SO<sub>2</sub> emissions and  $\pm 2\%$  for total anthropogenic NO<sub>x</sub> emissions. However, the differences  
between the separate and joint inversions are up to 100% and 40% in some model grid cells for anthropogenic  
SO<sub>2</sub> and NO<sub>x</sub> emissions, respectively. In comparison to OMPS observations, NCRMSE from joint inversions ( $\gamma$   
in the range of 200 to 2000) is reduced by ~45%~60% for SO<sub>2</sub> and ~38%~50% for NO<sub>2</sub>, respectively, which is  
560 close to the ~60% reduction from the SO<sub>2</sub> inversion and the ~50% reduction from the separate NO<sub>2</sub> inversion. To  
obtain posterior emissions for both SO<sub>2</sub> and NO<sub>x</sub>, the computational time for the joint inversion is only about ~50%

of the single-species inversions, when the latter are computed sequentially. Moreover, posterior GEOS-Chem SO<sub>2</sub> and NO<sub>2</sub> show improvements in terms of R when comparing against OMI observations, and the increase of posterior GEOS-Chem NO<sub>2</sub> negative NMB is ascribed to that the average of OMPS NO<sub>2</sub> over China is smaller than the OMI counterpart. Above all, the posterior emission increases the GEOS-Chem simulated spatial distributions of SO<sub>2</sub> and NO<sub>2</sub>.

Both data quality control and spatially balancing the cost function play an important role for constraining SO<sub>2</sub> emissions. OMPS SO<sub>2</sub> retrievals over the regions where emissions are small are removed as VCDs are comparable to retrieval errors. A sensitivity study shows that if these data are included, it will lead to artifacts in the posterior SO<sub>2</sub> emission spatial distribution. Due to cloud screening, the number of OMPS SO<sub>2</sub> retrievals over the Sichuan Basin is much less than that over the North China Plain, which will lead to under-constraining over Sichuan Basin, if the observation error is assumed spatially constant. When the observation error is set based on the number of observations, the artifacts are avoided.

575

To investigate the impacts of the uncertainty of NH<sub>3</sub> emissions on posterior SO<sub>2</sub> and NO<sub>x</sub> emissions, several inverse modeling experiments are conducted by setting prior NH<sub>3</sub> emissions to as 50% and 20% of their original values. The reduction of NH<sub>3</sub> emissions can lead to a larger decrease of posterior NO<sub>x</sub> emissions and a smaller decrease of SO<sub>2</sub> emissions in separate assimilations, which ascribes to the NO<sub>2</sub> lifetime is more than the SO<sub>2</sub> affected by the change of NH<sub>3</sub> emissions. The impacts of NH<sub>3</sub> emissions uncertainty on both posterior SO<sub>2</sub> and NO<sub>x</sub> emissions in joint assimilations are stronger than separate assimilations.

Large SO<sub>2</sub> emissions are mainly produced over the Sichuan basin and the North China Plain, while AOD responses to the changes of SO<sub>2</sub> emissions are quite different over the two regions. The reduction in SO<sub>2</sub> emissions can effectively decrease AOD over the Sichuan Basin, while AOD declines only slightly over the North China Plain, which can be ascribed to (1) nitrate rather than sulfate is dominant over the North China Plain and (2) the reduction of SO<sub>2</sub> emissions facilitate the formation of additional nitrate. AOD over the North China Plain is mainly determined by NO<sub>x</sub> and NH<sub>3</sub> emissions rather than SO<sub>2</sub> emissions.

All emissions are constrained on the monthly scale and at the coarse spatial resolution of 2°×2.5° in this study, as OMPS observations are provided once per day at the resolutions as coarse as 50 × 50 km<sup>2</sup> at nadir and 50 × 190 km<sup>2</sup> at edge and the 4D-Var data assimilation at finer spatial resolution (on the order of 0.1 degree) would be

computationally prohibitive. The approach, however, has the potential for optimizing emissions [at daily to weekly scale and in fine spatial resolution \(on order of ~ 10 km\) from future satellite observations at high spatial and temporal resolutions](#). In particular, TEMPO (monitoring North America), GEMS (monitoring East Asia), and Sentinel-4 (monitoring Europe) are to be launched in the next several years, and all of these satellites will provide hourly SO<sub>2</sub> and NO<sub>2</sub> observations during the daytime [with resolution of 2.1 × 4.4 km<sup>2</sup>, 7 × 8 km<sup>2</sup>, 8.9 × 11.7 km<sup>2</sup>, respectively](#). Furthermore, in Part II of this work, we develop various downscale methods to apply these coarser-resolution top-down estimates of emissions for air quality forecasts and evaluate the forecasts with surface measurements, both at the finer spatial scale (Wang et al., 2019).

Author contributions. All authors designed the research; YW conducted the research; YW and JW wrote the paper; XX, DKH and ZQ contributed to writing.

Competing interests. The authors declare that they have no conflict of interest.

Acknowledgements. This research is supported by the National Aeronautics and Space Administration (NASA) through [Aura program managed by Kenneth W. Jucks](#), ACMAP program (grant numbers: NNX17AF77G and 80NSSC19K0950) managed by Richard Eckman, and through TEMPO project as part of NASA's Earth Venture program (grant number SV7-87011 subcontracted from Harvard Smithsonian Observatory to the University of Iowa). We acknowledge the computational support from the High-Performance Computing group at The University of Iowa and Prof. Charles O. Stanier from The University of Iowa for insightful comments on the analysis of SO<sub>2</sub> and NO<sub>2</sub> lifetimes.

## References

- [Bannister, R. N.: A review of forecast error covariance statistics in atmospheric variational data assimilation. I: Characteristics and measurements of forecast error covariances, Quarterly Journal of the Royal Meteorological Society, 134, 1951-1970, 10.1002/qj.339, 2008.](#)
- [Benedetti, A., and Fisher, M.: Background error statistics for aerosols, Quarterly Journal of the Royal Meteorological Society, 133, 391-405, 10.1002/qj.37, 2007.](#)
- [Bucsela, E. J., Celarier, E. A., Gleason, J. L., Krotkov, N. A., Lamsal, L. N., Marchenko, S. V., and Swartz, W. H.: OMNO2 README Document Data Product Version 3.0, 2016.](#)

- Byrd, R., Lu, P., Nocedal, J., and Zhu, C.: A Limited Memory Algorithm for Bound Constrained Optimization, *SIAM J. Sci. Comput.*, 16, 1190-1208, doi:10.1137/0916069, 1995.
- 625 Calkins, C., Ge, C., Wang, J., Anderson, M., and Yang, K.: Effects of meteorological conditions on sulfur dioxide air pollution in the North China plain during winters of 2006–2015, *Atmos. Environ.*, 147, 296-309, <https://doi.org/10.1016/j.atmosenv.2016.10.005>, 2016.
- Cooper, M., Martin, R. V., Padmanabhan, A., and Henze, D. K.: Comparing mass balance and adjoint methods for inverse modeling of nitrogen dioxide columns for global nitrogen oxide emissions, *J. Geophys. Res.*, 122, 4718-4734, 10.1002/2016JD025985, 2017.
- 630 Ding, J., Miyazaki, K., van der A, R. J., Mijling, B., Kurokawa, J. I., Cho, S., Janssens-Maenhout, G., Zhang, Q., Liu, F., and Levelt, P. F.: Intercomparison of NO<sub>x</sub> emission inventories over East Asia, *Atmos. Chem. Phys.*, 17, 10125-10141, 10.5194/acp-17-10125-2017, 2017.
- Ding, J., van der A, R. J., Mijling, B., Levelt, P. F., and Hao, N.: NO<sub>x</sub> emission estimates during the 2014 Youth Olympic Games in Nanjing, *Atmos. Chem. Phys.*, 15, 9399-9412, 10.5194/acp-15-9399-2015, 2015.
- 635 Fioletov, V. E., McLinden, C. A., Krotkov, N., Yang, K., Loyola, D. G., Valks, P., Theys, N., Van Roozendael, M., Nowlan, C. R., Chance, K., Liu, X., Lee, C., and Martin, R. V.: Application of OMI, SCIAMACHY, and GOME-2 satellite SO<sub>2</sub> retrievals for detection of large emission sources, *J. Geophys. Res.*, 118, 2013JD019967, 10.1002/jgrd.50826, 2013.
- Fioletov, V. E., McLinden, C. A., Krotkov, N., Li, C., Joiner, J., Theys, N., Carn, S., and Moran, M. D.: A global catalogue of large SO<sub>2</sub> sources and emissions derived from the Ozone Monitoring Instrument, *Atmos. Chem. Phys.*, 16, 11497-11519, 10.5194/acp-16-11497-2016, 2016.
- 640 Flynn, L., Long, C., Wu, X., Evans, R., Beck, C. T., Petropavlovskikh, I., McConville, G., Yu, W., Zhang, Z., Niu, J., Beach, E., Hao, Y., Pan, C., Sen, B., Novicki, M., Zhou, S., and Seftor, C.: Performance of the Ozone Mapping and Profiler Suite (OMPS) products, *J. Geophys. Res.*, 119, 6181-6195, 10.1002/2013JD020467, 2014.
- 645 Henze, D. K., Hakami, A., and Seinfeld, J. H.: Development of the adjoint of GEOS-Chem, *Atmos. Chem. Phys.*, 7, 2413-2433, 10.5194/acp-7-2413-2007, 2007.
- Hollingsworth, A., and Lönnberg, P.: The statistical structure of short-range forecast errors as determined from radiosonde data. Part I: The wind field, *Tellus A*, 38A, 111-136, 10.1111/j.1600-0870.1986.tb00460.x, 1986.
- 650 Janssens-Maenhout, G., Crippa, M., Guizzardi, D., Dentener, F., Muntean, M., Pouliot, G., Keating, T., Zhang, Q., Kurokawa, J., Wankmüller, R., Denier van der Gon, H., Kuenen, J. J. P., Klimont, Z., Frost, G.,

- 655 Darras, S., Koffi, B., and Li, M.: HTAP\_v2.2: a mosaic of regional and global emission grid maps for 2008 and 2010 to study hemispheric transport of air pollution, *Atmos. Chem. Phys.*, 15, 11411-11432, 10.5194/acp-15-11411-2015, 2015.
- Kharol, S. K., Martin, R. V., Philip, S., Vogel, S., Henze, D. K., Chen, D., Wang, Y., Zhang, Q., and Heald, C. L.: Persistent sensitivity of Asian aerosol to emissions of nitrogen oxides, *Geophys. Res. Lett.*, 40, 1021-1026, 10.1002/grl.50234, 2013.
- 660 Kong, H., Lin, J., Zhang, R., Liu, M., Weng, H., Ni, R., Chen, L., Wang, J., and Zhang, Q.: High-resolution ( $0.05^\circ \times 0.05^\circ$ ) NO<sub>x</sub> emissions in the Yangtze River Delta inferred from OMI, *Atmos. Chem. Phys. Discuss.*, 2019, 1-39, 10.5194/acp-2018-1275, 2019.
- Koukouli, M. E., Theys, N., Ding, J., Zyrichidou, I., Mijling, B., Balis, D., and van der A, R. J.: Updated SO<sub>2</sub> emission estimates over China using OMI/Aura observations, *Atmos. Meas. Tech.*, 11, 1817-1832, 10.5194/amt-11-1817-2018, 2018.
- 665 Krotkov, N. A., Lamsal, L. N., Celarier, E. A., Swartz, W. H., Marchenko, S. V., Bucsela, E. J., Chan, K. L., Wenig, M., and Zara, M.: The version 3 OMI NO<sub>2</sub> standard product, *Atmos. Meas. Tech.*, 10, 3133-3149, 10.5194/amt-10-3133-2017, 2017.
- Kurokawa, J., Ohara, T., Morikawa, T., Hanayama, S., Janssens-Maenhout, G., Fukui, T., Kawashima, K., and Akimoto, H.: Emissions of air pollutants and greenhouse gases over Asian regions during 2000–2008: Regional Emission inventory in ASia (REAS) version 2, *Atmos. Chem. Phys.*, 13, 11019-11058, 10.5194/acp-13-11019-2013, 2013.
- 670 Kurokawa, J.-i., Yumimoto, K., Uno, I., and Ohara, T.: Adjoint inverse modeling of NO<sub>x</sub> emissions over eastern China using satellite observations of NO<sub>2</sub> vertical column densities, *Atmos. Environ.*, 43, 1878-1887, <http://dx.doi.org/10.1016/j.atmosenv.2008.12.030>, 2009.
- 675 Lamsal, L. N., Martin, R. V., van Donkelaar, A., Celarier, E. A., Bucsela, E. J., Boersma, K. F., Dirksen, R., Luo, C., and Wang, Y.: Indirect validation of tropospheric nitrogen dioxide retrieved from the OMI satellite instrument: Insight into the seasonal variation of nitrogen oxides at northern midlatitudes, *J. Geophys. Res.*, 115, 10.1029/2009JD013351, 2010.
- 680 Lamsal, L. N., Martin, R. V., Padmanabhan, A., van Donkelaar, A., Zhang, Q., Sioris, C. E., Chance, K., Kurosu, T. P., and Newchurch, M. J.: Application of satellite observations for timely updates to global anthropogenic NO<sub>x</sub> emission inventories, *Geophys. Res. Lett.*, 38, L05810, 10.1029/2010GL046476, 2011.

- 685 Lee, C., Martin, R. V., van Donkelaar, A., Lee, H., Dickerson, R. R., Hains, J. C., Krotkov, N., Richter, A.,  
Vinnikov, K., and Schwab, J. J.: SO<sub>2</sub> emissions and lifetimes: Estimates from inverse modeling using in  
situ and global, space-based (SCIAMACHY and OMI) observations, *J. Geophys. Res.*, 116, D06304,  
10.1029/2010JD014758, 2011.
- Lelieveld, J., Evans, J. S., Fnais, M., Giannadaki, D., and Pozzer, A.: The contribution of outdoor air pollution  
sources to premature mortality on a global scale, *Nature*, 525, 367-371, 10.1038/nature15371, 2015.
- Leonard, J. T.: README for OMSO2e (OMI Daily L3e for OMSO2) Version 1.1.7,  
690 [https://acd-disc.gesdisc.eosdis.nasa.gov/data/Aura\\_OMI\\_Level3/OMSO2e.003/doc/README.OMSO2e.  
pdf](https://acd-disc.gesdisc.eosdis.nasa.gov/data/Aura_OMI_Level3/OMSO2e.003/doc/README.OMSO2e.pdf), 2017.
- Li, C., Joiner, J., Krotkov, N. A., and Bhartia, P. K.: A fast and sensitive new satellite SO<sub>2</sub> retrieval algorithm  
based on principal component analysis: Application to the ozone monitoring instrument, *Geophys. Res.  
Lett.*, 40, 6314-6318, 10.1002/2013GL058134, 2013.
- 695 Li, C., Krotkov, N. A., Carn, S., Zhang, Y., Spurr, R. J. D., and Joiner, J.: New-generation NASA Aura Ozone  
Monitoring Instrument (OMI) volcanic SO<sub>2</sub> dataset: algorithm description, initial results, and  
continuation with the Suomi-NPP Ozone Mapping and Profiler Suite (OMPS), *Atmos. Meas. Tech.*, 10,  
445-458, 10.5194/amt-10-445-2017, 2017a.
- Li, M., Zhang, Q., Kurokawa, J. I., Woo, J. H., He, K., Lu, Z., Ohara, T., Song, Y., Streets, D. G., Carmichael, G.  
700 R., Cheng, Y., Hong, C., Huo, H., Jiang, X., Kang, S., Liu, F., Su, H., and Zheng, B.: MIX: a mosaic  
Asian anthropogenic emission inventory under the international collaboration framework of the MICS-  
Asia and HTAP, *Atmos. Chem. Phys.*, 17, 935-963, 10.5194/acp-17-935-2017, 2017b.
- Lim, S. S., Vos, T., Flaxman, A. D., Danaei, G., Shibuya, K., Adair-Rohani, H., AlMazroa, M. A., Amann, M.,  
Anderson, H. R., Andrews, K. G., Aryee, M., Atkinson, C., Bacchus, L. J., Bahalim, A. N., Balakrishnan,  
705 K., Balmes, J., Barker-Collo, S., Baxter, A., Bell, M. L., Blore, J. D., Blyth, F., Bonner, C., Borges, G.,  
Bourne, R., Boussinesq, M., Brauer, M., Brooks, P., Bruce, N. G., Brunekreef, B., Bryan-Hancock, C.,  
Bucello, C., Buchbinder, R., Bull, F., Burnett, R. T., Byers, T. E., Calabria, B., Carapetis, J., Carnahan,  
E., Chafe, Z., Charlson, F., Chen, H., Chen, J. S., Cheng, A. T.-A., Child, J. C., Cohen, A., Colson, K.  
E., Cowie, B. C., Darby, S., Darling, S., Davis, A., Degenhardt, L., Dentener, F., Des Jarlais, D. C.,  
710 Devries, K., Dherani, M., Ding, E. L., Dorsey, E. R., Driscoll, T., Edmond, K., Ali, S. E., Engell, R. E.,  
Erwin, P. J., Fahimi, S., Falder, G., Farzadfar, F., Ferrari, A., Finucane, M. M., Flaxman, S., Fowkes, F.  
G. R., Freedman, G., Freeman, M. K., Gakidou, E., Ghosh, S., Giovannucci, E., Gmel, G., Graham, K.,  
Grainger, R., Grant, B., Gunnell, D., Gutierrez, H. R., Hall, W., Hoek, H. W., Hogan, A., Hosgood Iii,



- 715 H. D., Hoy, D., Hu, H., Hubbell, B. J., Hutchings, S. J., Ibeanusi, S. E., Jacklyn, G. L., Jasrasaria, R.,  
Jonas, J. B., Kan, H., Kanis, J. A., Kassebaum, N., Kawakami, N., Khang, Y.-H., Khatibzadeh, S., Khoo,  
J.-P., Kok, C., Laden, F., Lalloo, R., Lan, Q., Lathlean, T., Leasher, J. L., Leigh, J., Li, Y., Lin, J. K.,  
Lipshultz, S. E., London, S., Lozano, R., Lu, Y., Mak, J., Malekzadeh, R., Mallinger, L., Marcenes, W.,  
March, L., Marks, R., Martin, R., McGale, P., McGrath, J., Mehta, S., Memish, Z. A., Mensah, G. A.,  
720 Merriman, T. R., Micha, R., Michaud, C., Mishra, V., Hanafiah, K. M., Mokdad, A. A., Morawska, L.,  
Mozaffarian, D., Murphy, T., Naghavi, M., Neal, B., Nelson, P. K., Nolla, J. M., Norman, R., Olives, C.,  
Omer, S. B., Orchard, J., Osborne, R., Ostro, B., Page, A., Pandey, K. D., Parry, C. D. H., Passmore, E.,  
Patra, J., Pearce, N., Pelizzari, P. M., Petzold, M., Phillips, M. R., Pope, D., Pope Iii, C. A., Powles, J.,  
Rao, M., Razavi, H., Rehfuess, E. A., Rehm, J. T., Ritz, B., Rivara, F. P., Roberts, T., Robinson, C.,  
725 Rodriguez-Portales, J. A., Romieu, I., Room, R., Rosenfeld, L. C., Roy, A., Rushton, L., Salomon, J. A.,  
Sampson, U., Sanchez-Riera, L., Sanman, E., Sapkota, A., Seedat, S., Shi, P., Shield, K., Shivakoti, R.,  
Singh, G. M., Sleet, D. A., Smith, E., Smith, K. R., Stapelberg, N. J. C., Steenland, K., Stöckl, H., Stovner,  
L. J., Straif, K., Straney, L., Thurston, G. D., Tran, J. H., Van Dingenen, R., van Donkelaar, A., Veerman,  
J. L., Vijayakumar, L., Weintraub, R., Weissman, M. M., White, R. A., Whiteford, H., Wiersma, S. T.,  
730 Wilkinson, J. D., Williams, H. C., Williams, W., Wilson, N., Woolf, A. D., Yip, P., Zielinski, J. M.,  
Lopez, A. D., Murray, C. J. L., and Ezzati, M.: A comparative risk assessment of burden of disease and  
injury attributable to 67 risk factors and risk factor clusters in 21 regions, 1990–2010: a systematic  
analysis for the Global Burden of Disease Study 2010, *The Lancet*, 380, 2224-2260,  
[http://dx.doi.org/10.1016/S0140-6736\(12\)61766-8](http://dx.doi.org/10.1016/S0140-6736(12)61766-8), 2012.
- 735 Liu, F., Zhang, Q., van der A., R., J., Zheng, B., Tong, D., Yan, L., Zheng, Y., and He, K.: Recent reduction in  
NO<sub>x</sub> emissions over China: synthesis of satellite observations and emission inventories, *Environ. Res.  
Lett.*, 11, 114002, 2016.
- Liu, F., Choi, S., Li, C., Fioletov, V. E., McLinden, C. A., Joiner, J., Krotkov, N. A., Bian, H., Janssens-Maenhout,  
G., Darmenov, A. S., and da Silva, A. M.: A new global anthropogenic SO<sub>2</sub> emission inventory for the  
last decade: a mosaic of satellite-derived and bottom-up emissions, *Atmos. Chem. Phys.*, 18, 16571-  
740 16586, 10.5194/acp-18-16571-2018, 2018.
- Liu, H., Jacob, D. J., Bey, I., and Yantosca, R. M.: Constraints from 210Pb and 7Be on wet deposition and  
transport in a global three-dimensional chemical tracer model driven by assimilated meteorological fields,  
*J. Geophys. Res.*, 106, 12109-12128, 10.1029/2000JD900839, 2001.

- 745 Liu, M., Huang, X., Song, Y., Tang, J., Cao, J., Zhang, X., Zhang, Q., Wang, S., Xu, T., Kang, L., Cai, X., Zhang, H., Yang, F., Wang, H., Yu, J. Z., Lau, A. K. H., He, L., Huang, X., Duan, L., Ding, A., Xue, L., Gao, J., Liu, B., and Zhu, T.: Ammonia emission control in China would mitigate haze pollution and nitrogen deposition, but worsen acid rain, *Proceedings of the National Academy of Sciences*, 201814880, 10.1073/pnas.1814880116, 2019.
- 750 Marchenko, S., Krotkov, N. A., Lamsal, L. N., Celarier, E. A., Swartz, W. H., and Bucsele, E. J.: Revising the slant column density retrieval of nitrogen dioxide observed by the Ozone Monitoring Instrument, *J. Geophys. Res.*, 120, 5670-5692, 10.1002/2014JD022913, 2015.
- Martin, R. V., Jacob, D. J., Chance, K., Kurosu, T. P., Palmer, P. I., and Evans, M. J.: Global inventory of nitrogen oxide emissions constrained by space-based observations of NO<sub>2</sub> columns, *J. Geophys. Res.*, 108, 4537, 10.1029/2003JD003453, 2003.
- 755 Mijling, B., and van der A, R. J.: Using daily satellite observations to estimate emissions of short-lived air pollutants on a mesoscopic scale, *J. Geophys. Res.*, 117, 10.1029/2012JD017817, 2012.
- Miyazaki, K., Eskes, H. J., and Sudo, K.: Global NO<sub>x</sub> emission estimates derived from an assimilation of OMI tropospheric NO<sub>2</sub> columns, *Atmos. Chem. Phys.*, 12, 2263-2288, 10.5194/acp-12-2263-2012, 2012.
- 760 Miyazaki, K., Eskes, H., Sudo, K., Boersma, K. F., Bowman, K., and Kanaya, Y.: Decadal changes in global surface NO<sub>x</sub> emissions from multi-constituent satellite data assimilation, *Atmos. Chem. Phys.*, 17, 807-837, 10.5194/acp-17-807-2017, 2017.
- Miyazaki, K., Eskes, H., Sudo, K., Boersma, K. F., Bowman, K., and Kanaya, Y.: Decadal changes in global surface NO<sub>x</sub> emissions from multi-constituent satellite data assimilation, *Atmos. Chem. Phys.*, 17, 807-837, 10.5194/acp-17-807-2017, 2017.
- 765 Myhre, G., Shindell, D., Bréon, F.-M., Collins, W., Fuglestedt, J., Huang, J., Koch, D., Lamarque, J.-F., Lee, D., Mendoza, B., Nakajima, T., Robock, A., Stephens, G., Takemura, T., and Zhang, H.: Anthropogenic and Natural Radiative Forcing, in: *Climate Change 2013: The Physical Science Basis. Contribution of Working Group I to the Fifth Assessment Report of the Intergovernmental Panel on Climate Change*, edited by: Stocker, T. F., Qin, D., Plattner, G.-K., Tignor, M., Allen, S. K., Boschung, J., Nauels, A., Xia, Y., Bex, V., and Midgley, P. M., Cambridge University Press, Cambridge, United Kingdom and New York, NY, USA, 659–740, 2013.
- 770 Park, R. J., Jacob, D. J., Field, B. D., Yantosca, R. M., and Chin, M.: Natural and transboundary pollution influences on sulfate-nitrate-ammonium aerosols in the United States: Implications for policy, *J. Geophys. Res.*, 109, D15204, 10.1029/2003JD004473, 2004.

- 775 Qu, Z., Henze, D. K., Capps, S. L., Wang, Y., Xu, X., Wang, J., and Keller, M.: Monthly top-down NO<sub>x</sub> emissions for China (2005–2012): A hybrid inversion method and trend analysis, *J. Geophys. Res.*, 122, 4600-4625, 10.1002/2016JD025852, 2017.
- Qu, Z., Henze, D. K., Li, C., Theys, N., Wang, Y., Wang, J., Wang, W., Han, J., Shim, C., Dickerson, R. R., and Ren, X.: SO<sub>2</sub> emission estimates using OMI SO<sub>2</sub> retrievals for 2005-2017, *J. Geophys. Res.*, 0, 10.1029/2019JD030243, 2019a.
- 780 Qu, Z., Henze, D. K., Theys, N., Wang, J., and Wang, W.: Hybrid mass balance/4D-Var joint inversion of NO<sub>x</sub> and SO<sub>2</sub> emissions in East Asia, *J. Geophys. Res.*, 0, 10.1029/2018JD030240, 2019b.
- Schenkeveld, V. M. E., Jaross, G., Marchenko, S., Haffner, D., Kleipool, Q. L., Rozemeijer, N. C., Veeffkind, J. P., and Levelt, P. F.: In-flight performance of the Ozone Monitoring Instrument, *Atmos. Meas. Tech.*, 10, 1957-1986, 10.5194/amt-10-1957-2017, 2017.
- 785 Seinfeld, J. H., and Pandis, S. N.: *Atmospheric Chemistry and Physics: From Air Pollution to Climate Change*, 3rd ed., Wiley, 2016.
- Taylor, K. E.: Summarizing multiple aspects of model performance in a single diagram, *J. Geophys. Res.*, 106, 7183-7192, 10.1029/2000JD900719, 2001.
- 790 Turner, A. J., Henze, D. K., Martin, R. V., and Hakami, A.: The spatial extent of source influences on modeled column concentrations of short-lived species, *Geophys. Res. Lett.*, 39, n/a-n/a, 10.1029/2012GL051832, 2012.
- Wang, Y., Jacob, D. J., and Logan, J. A.: Global simulation of tropospheric O<sub>3</sub>-NO<sub>x</sub>-hydrocarbon chemistry: 1. Model formulation, *J. Geophys. Res.*, 103, 10713-10725, 10.1029/98JD00158, 1998.
- 795 Wang, Y., Zhang, Q. Q., He, K., Zhang, Q., and Chai, L.: Sulfate-nitrate-ammonium aerosols over China: response to 2000–2015 emission changes of sulfur dioxide, nitrogen oxides, and ammonia, *Atmos. Chem. Phys.*, 13, 2635-2652, 10.5194/acp-13-2635-2013, 2013.
- Wang, Y., and Wang, J.: Tropospheric SO<sub>2</sub> and NO<sub>2</sub> in 2012–2018: Contrasting views of two sensors (OMI and OMPS) from space, *Atmos. Environ.*, 223, 117214, <https://doi.org/10.1016/j.atmosenv.2019.117214>, 2020.
- 800 Wang, Y., Wang, J., Xu, X., Henze, D. K., Wang, Y., and Qu, Z.: A new approach for monthly updates of anthropogenic sulfur dioxide emissions from space: Application to China and implications for air quality forecasts, *Geophys. Res. Lett.*, 43, 9931-9938, 10.1002/2016GL070204, 2016.

- 805 Wang, Y., Wang, J., Henze, D. K., Zhou, M., Ge, C., and Wang, W.: Inverse modeling of SO<sub>2</sub> and NO<sub>x</sub> emissions  
over China from multi-sensor satellite data: 2. Downscaling for air quality forecasts *Atmos. Chem. Phys.*,  
2019.(submitted)
- Wesely, M. L.: Parameterization of surface resistances to gaseous dry deposition in regional-scale numerical  
models, *Atmospheric Environment* (1967), 23, 1293-1304, [http://dx.doi.org/10.1016/0004-  
6981\(89\)90153-4](http://dx.doi.org/10.1016/0004-6981(89)90153-4), 1989.
- 810 Xu, X., Wang, J., Henze, D. K., Qu, W., and Kopacz, M.: Constraints on aerosol sources using GEOS-Chem  
adjoint and MODIS radiances, and evaluation with multisensor (OMI, MISR) data, *J. Geophys. Res.*,  
118, 6396-6413, 10.1002/jgrd.50515, 2013.
- [Xu, X., Wang, J., Zeng, J., Spurr, R., Liu, X., Dubovik, O., et al. \(2015\). Retrieval of aerosol microphysical properties  
from AERONET photopolarimetric measurements: 2. A new research algorithm and case demonstration.  
815 \*Journal of Geophysical Research: Atmospheres\*, 120\(14\), 2015JD023113.](#)
- Yang, K., Dickerson, R. R., Carn, S. A., Ge, C., and Wang, J.: First observations of SO<sub>2</sub> from the satellite Suomi  
NPP OMPS: Widespread air pollution events over China, *Geophys. Res. Lett.*, 40, 4957-4962,  
10.1002/grl.50952, 2013.
- Yang, K., Carn, S. A., Ge, C., Wang, J., and Dickerson, R. R.: Advancing measurements of tropospheric NO<sub>2</sub>  
820 from space: New algorithm and first global results from OMPS, *Geophys. Res. Lett.*, 41, 4777-4786,  
10.1002/2014GL060136, 2014.
- Zhang, Y., Li, C., Krotkov, N. A., Joiner, J., Fioletov, V., and McLinden, C.: Continuation of long-term global  
SO<sub>2</sub> pollution monitoring from OMI to OMPS, *Atmos. Meas. Tech.*, 10, 1495-1509, 10.5194/amt-10-  
1495-2017, 2017.
- 825 Zheng, B., Tong, D., Li, M., Liu, F., Hong, C., Geng, G., Li, H., Li, X., Peng, L., Qi, J., Yan, L., Zhang, Y., Zhao,  
H., Zheng, Y., He, K., and Zhang, Q.: Trends in China's anthropogenic emissions since 2010 as the  
consequence of clean air actions, *Atmos. Chem. Phys.*, 18, 14095-14111, 10.5194/acp-18-14095-2018,  
2018.

830

**Table 1. Different experimental design for using OMPS SO<sub>2</sub> and NO<sub>2</sub> to constrain corresponding emissions over China for October 2013.**

Name	Data	SO <sub>2</sub> error <sup>b</sup>	NO <sub>2</sub> error	$\gamma^c$	QC for SO <sub>2</sub> <sup>d</sup>
E-SO <sub>2</sub>	SO <sub>2</sub>	0.2 DU x $\sqrt{N}$	NA	1	Yes
E-NO <sub>2</sub>	NO <sub>2</sub>	NA	0.011 DU	NA	NA
E-joint	SO <sub>2</sub> and NO <sub>2</sub>	0.2 DU x $\sqrt{N}$	0.011 DU	200	Yes
E-SO <sub>2</sub> -noQC-noBL	SO <sub>2</sub>	0.2 DU	NA	1	No
E-SO <sub>2</sub> -noBL	SO <sub>2</sub>	0.2 DU	NA	1	Yes
E-joint-d $\gamma$	SO <sub>2</sub> and NO <sub>2</sub>	0.2 DU x $\sqrt{N}$	0.011 DU	20 to 2000 <sup>e</sup>	Yes

<sup>a</sup>See description of these names in detail in Set. 3.2.

<sup>b</sup> $N$  in this column is number of OMPS overpass that have SO<sub>2</sub> observation in the 2x2.5 GEOS-Chem grid cell.

835 <sup>c</sup> $\gamma$  is a parameter used to balance SO<sub>2</sub> and NO<sub>2</sub> observation terms in the cost function.

<sup>d</sup>OMPS SO<sub>2</sub> retrievals in the 2x2.5 grid cell where the prior GEOS-Chem simulation is less than 0.1 DU are removed.

<sup>e</sup>All these  $\gamma$  values (20, 50, 100, 300, 500, 1000, 1500, and 2000) are used.

840

**Table 2. Different experimental design for assessing the impacts of NH<sub>3</sub> emission inventories on using OMPS SO<sub>2</sub> and NO<sub>2</sub> to constrain corresponding emissions over China for October 2013<sup>a</sup>.**

Name <sup>b</sup>	Data	$\gamma$ <sup>c</sup>	NH <sub>3</sub> emissions
E-SO <sub>2</sub> -0.5NH <sub>3</sub>	SO <sub>2</sub>	NA	50%
E-NO <sub>2</sub> -0.5NH <sub>3</sub>	NO <sub>2</sub>	NA	50%
E-joint-0.5NH <sub>3</sub> - $\gamma$ 500	SO <sub>2</sub> and NO <sub>2</sub>	500	50%
E-SO <sub>2</sub> -0.2NH <sub>3</sub>	SO <sub>2</sub>	NA	20%
E-NO <sub>2</sub> -0.2NH <sub>3</sub>	NO <sub>2</sub>	NA	20%
E-joint-0.2NH <sub>3</sub> - $\gamma$ 500	SO <sub>2</sub> and NO <sub>2</sub>	500	20%

<sup>a</sup>Data quality control and observation errors are same as E-joint in Table 1.

<sup>b</sup>See description of these names in detail in Set. 3.2.

845 <sup>c</sup> $\gamma$  is a parameter used to balance SO<sub>2</sub> and NO<sub>2</sub> observation terms in the cost function.

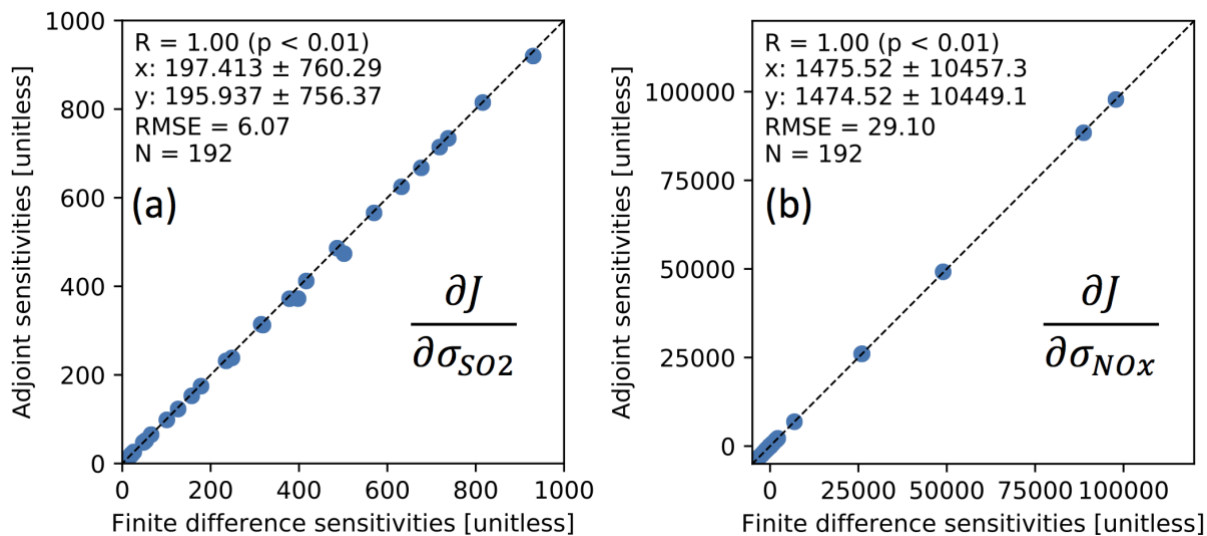
**Table 3. Posterior anthropogenic emissions for October 2013 from E-joint, E-joint-d $\gamma$ , E-SO<sub>2</sub> and E-NO<sub>2</sub>.**

Experiment name or $\gamma$	20	50	100	200	300	500	1000	1500	2000	E-SO <sub>2</sub> or E-NO <sub>2</sub>
SO <sub>2</sub> [Gg S]	1143	1110	1055	860	795	802	733	730	728	748
NO <sub>x</sub> [Gg N]	681	682	682	667	662	664	668	666	674	672

**Table 4. Posterior anthropogenic emissions for October 2013 under different NH<sub>3</sub> emission scenarios**

Name	SO <sub>2</sub> emissions [Gg S]	NO <sub>x</sub> emission [Gg N]
E-SO <sub>2</sub>	748	NA
E-SO <sub>2</sub> -0.5NH <sub>3</sub>	747	NA
E-SO <sub>2</sub> -0.2NH <sub>3</sub>	745	NA
E-NO <sub>2</sub>	NA	672
E-NO <sub>2</sub> -0.5NH <sub>3</sub>	NA	667
E-NO <sub>2</sub> -0.2NH <sub>3</sub>	NA	653
E-joint-d $\gamma$ ( $\gamma=500$ )	802	664
E-joint-0.5NH <sub>3</sub> - $\gamma$ 500	783	646
E-joint-0.2NH <sub>3</sub> - $\gamma$ 500	746	629





855 **Figure 1. Validation of adjoint model sensitivity through comparison to centered finite difference results for a 3-day simulation. Shown here are the sensitivity of column cost function (penalty term is not included, and horizontal transport is turned off) with respect to logarithm of anthropogenic SO<sub>2</sub> (a) and NO<sub>x</sub> (b) emission scale factors: the 1:1 line (dotted), the number of grid columns (N), Root Mean Squared Error (RMSE), and correlation coefficient (R), and Means and standard deviations of finite difference sensitivity and adjoint sensitivity (x and y).**

860

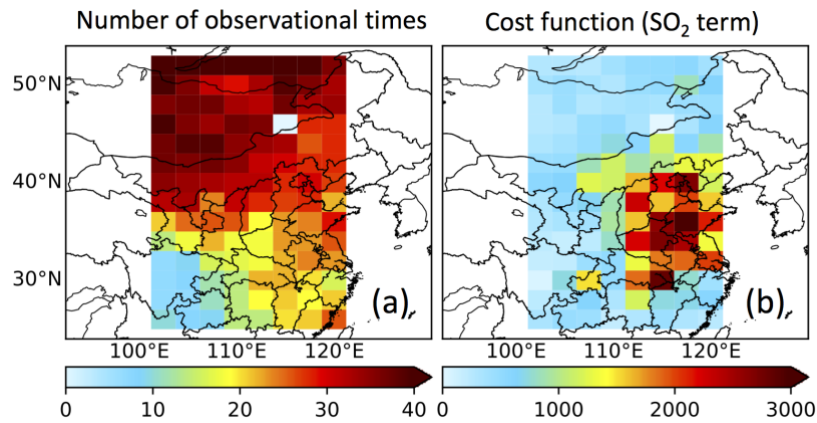
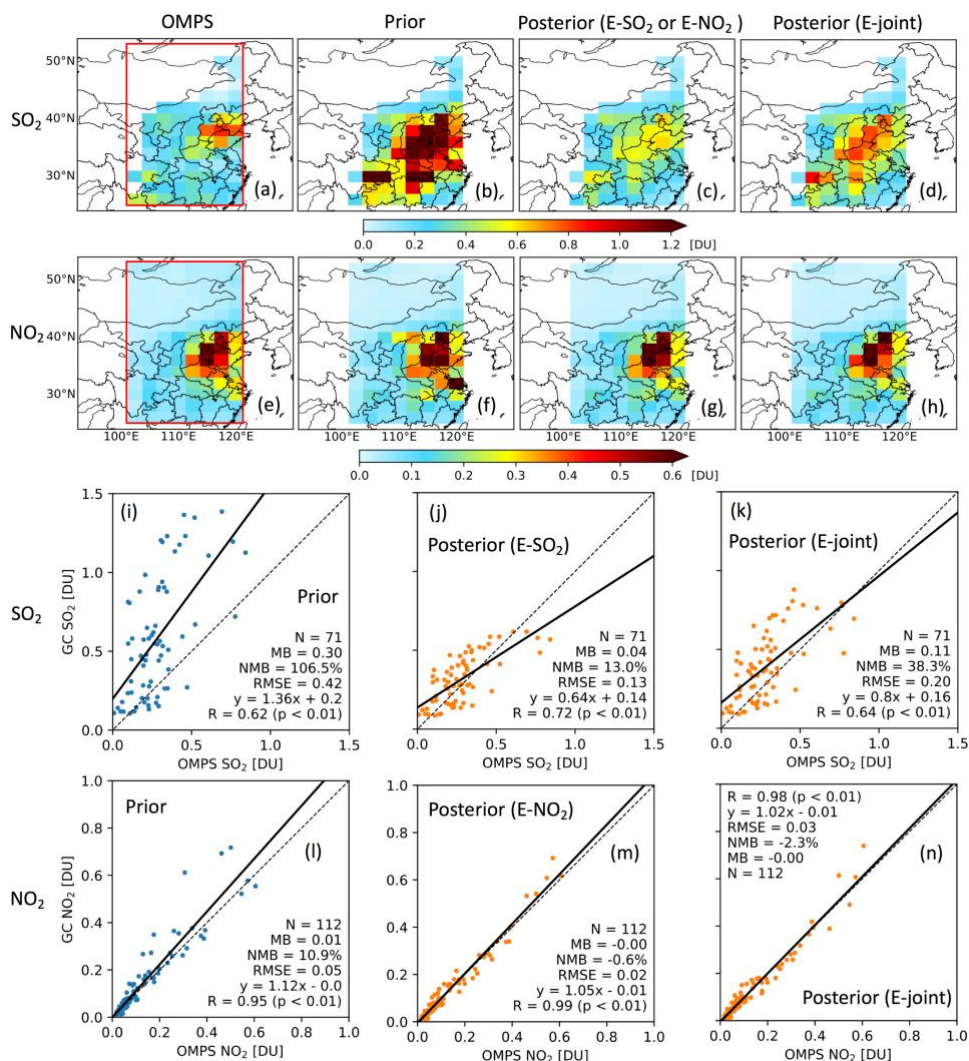


**Figure 2.** (a) and (b) are the numbers of the OMPS overpass time that provides SO<sub>2</sub> VCD retrievals and SO<sub>2</sub> term in cost function at first iteration, respectively, in October 2013

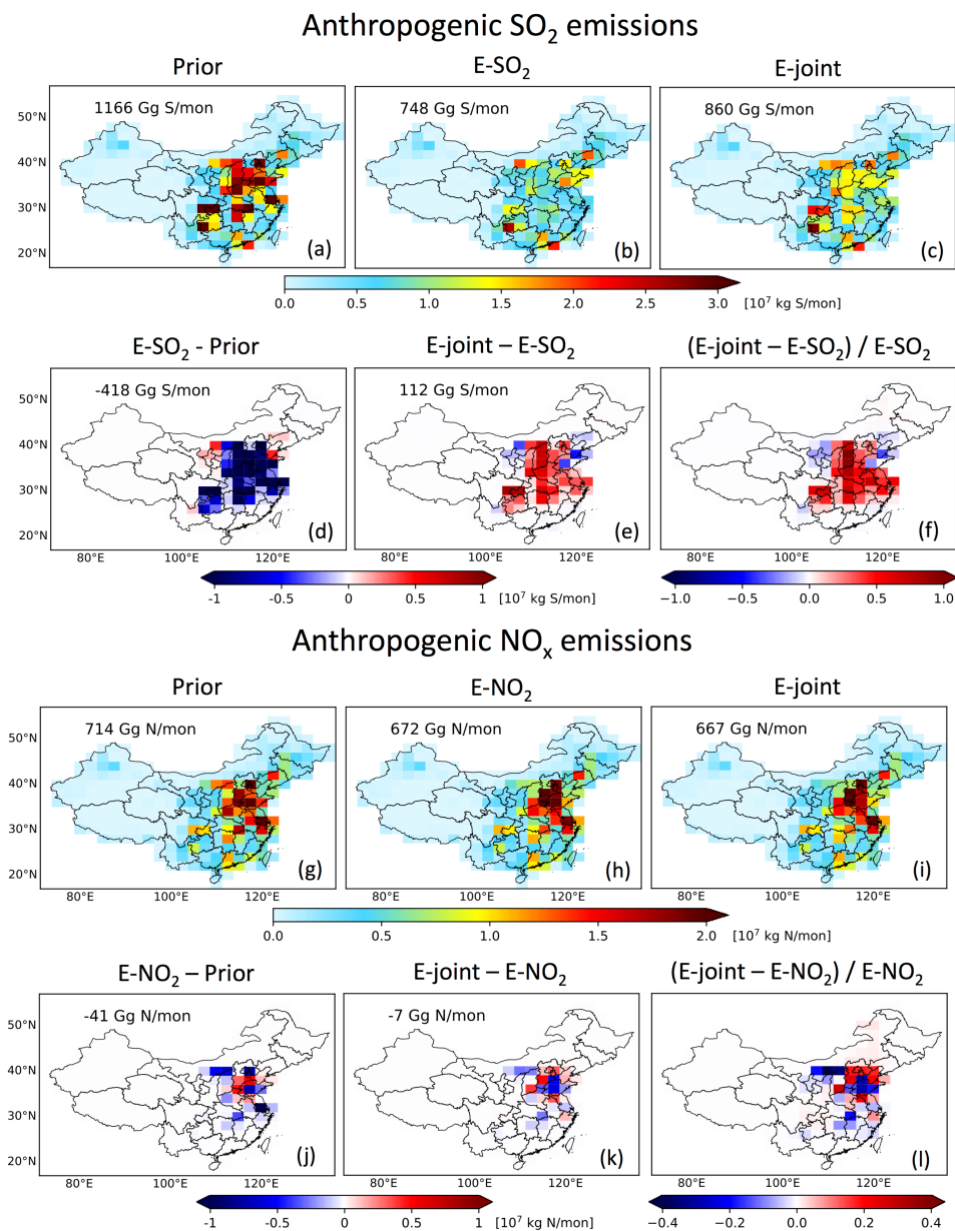


865

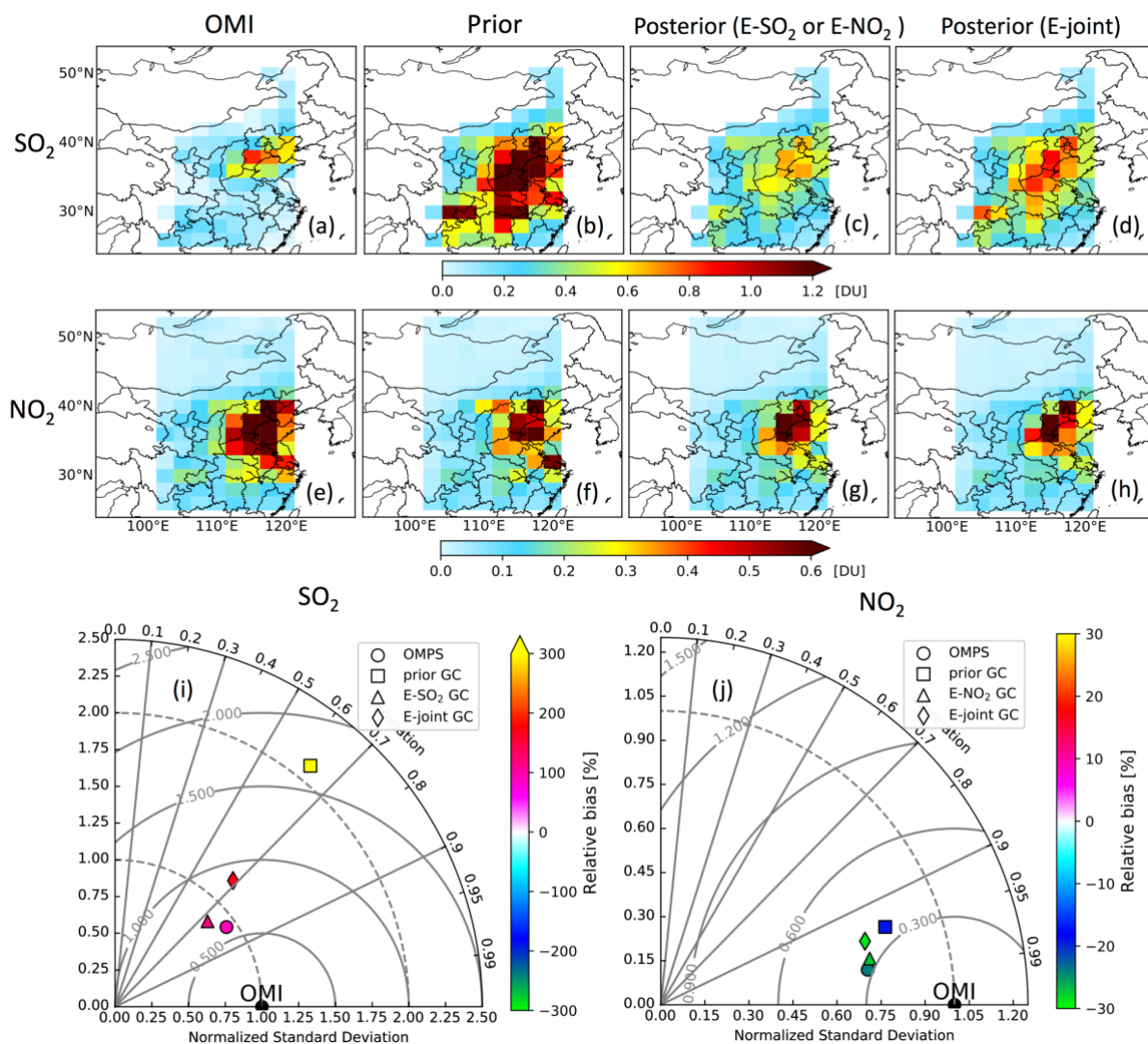
870

875

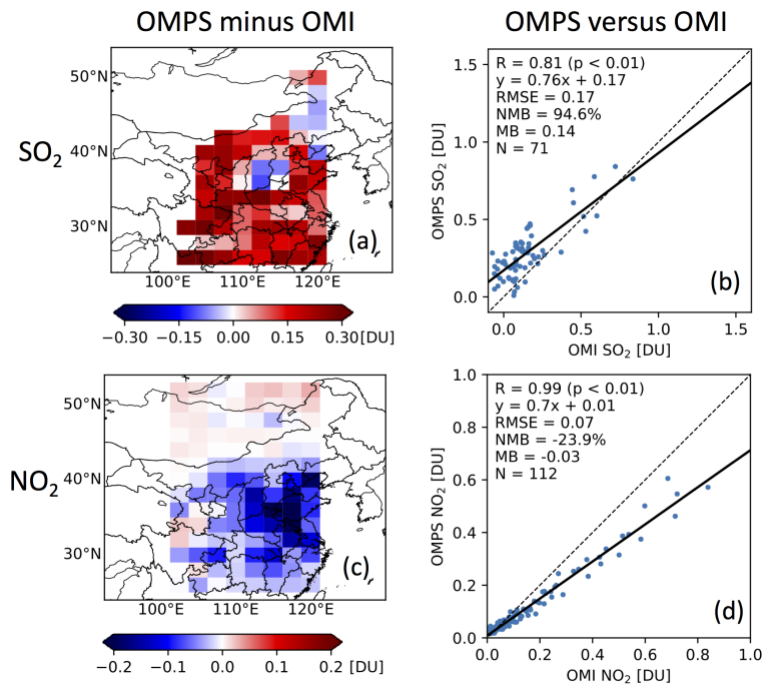
Figure 3. Comparisons of VCDs of SO<sub>2</sub> and NO<sub>2</sub> from the OMPS and the GEOS-Chem prior and posterior simulations in October 2013 over China. The first row is SO<sub>2</sub> VCDs from the OMPS (a), the prior simulation (b), the E-SO<sub>2</sub> posterior simulation (c), and the E-joint posterior simulation (d). The second row is NO<sub>2</sub> tropospheric VCDs from the OMPS (e), the prior simulation (f), the E-NO<sub>2</sub> posterior simulation (g), and the E-joint posterior simulation (h). The third row is the SO<sub>2</sub> VCD scatter plots of the GEOS-Chem prior (i), the E-SO<sub>2</sub> posterior (j), and the E-joint posterior (k) versus the OMPS, respectively. The last row is the NO<sub>2</sub> tropospheric VCD scatter plots of the GEOS-Chem prior (l), the E-NO<sub>2</sub> posterior (m), and the E-joint posterior (n) versus the OMPS, respectively. Linear correlation coefficient (R), linear regression equation, root mean squared error (RMSE), normalized mean bias (NMB), mean bias (MB), and number of observations (N) are shown over scatter plots.



880 **Figure 4.** The top is anthropogenic SO<sub>2</sub> emissions from prior MIX 2010 (a), posterior E-SO<sub>2</sub> (b), posterior E-joint (c), the difference between posterior E-SO<sub>2</sub> and prior MIX 2010 (d), the difference between posterior E-joint and posterior E-SO<sub>2</sub> (e), and the relative difference between posterior E-joint and posterior E-SO<sub>2</sub> (f) for October 2013. The bottom is similar to the top except that (1) it is for NO<sub>x</sub> and (2) E-SO<sub>2</sub> is replaced by E-NO<sub>2</sub>.



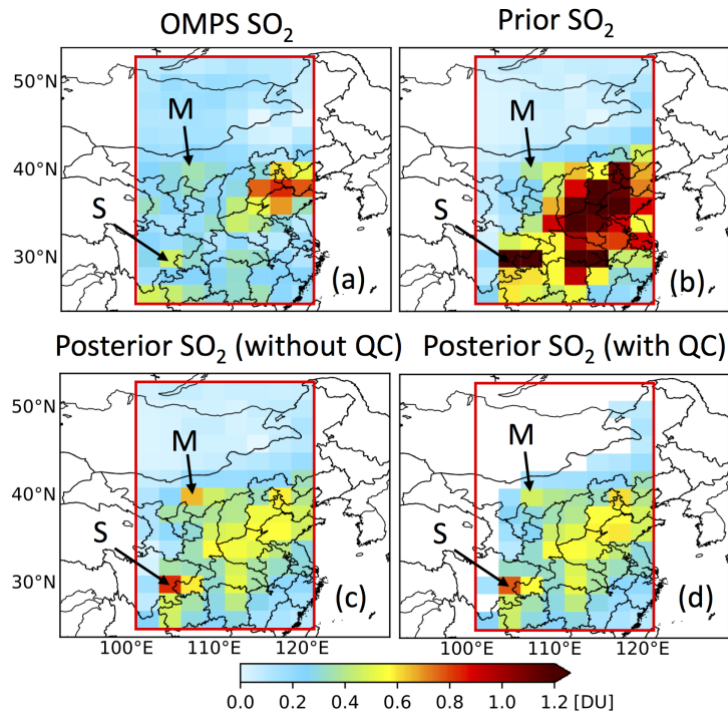
885 Figure 5. Comparisons of VCDs of  $\text{SO}_2$  and  $\text{NO}_2$  from the OMPS and the GEOS-Chem prior and posterior simulations  
 with that from the OMI in October 2013 over China. The first row is  $\text{SO}_2$  VCDs from the OMI (a), the prior simulation  
 (b), the E- $\text{SO}_2$  posterior simulation (c), and the E-joint posterior simulation (d). The second row is  $\text{NO}_2$  tropospheric  
 890 VCDs from the OMI (e), the prior simulation (f), the E- $\text{NO}_2$  posterior simulation (g), and the E-joint posterior  
 simulation (h). The third row is Taylor diagrams for comparing GEOS-Chem simulations (squares for prior, triangles  
 for posterior E- $\text{SO}_2$  or E- $\text{NO}_2$ , and diamonds for E-joint) and OMPS observations (circles) with OMI  $\text{SO}_2$  (i) and  $\text{NO}_2$   
 (j).



895 **Figure 6. (a) and (b) are the difference between OMPS and OMI SO<sub>2</sub> and scatter plot of OMPS versus OMI SO<sub>2</sub>. (c) and (d) are similar (a) and (b), but for NO<sub>2</sub>. Linear correlation coefficient (R), linear regression equation, root mean squared error (RMSE), normalized mean bias (NMB), mean bias (MB), and number of observations (N) are shown over scatter plots.**

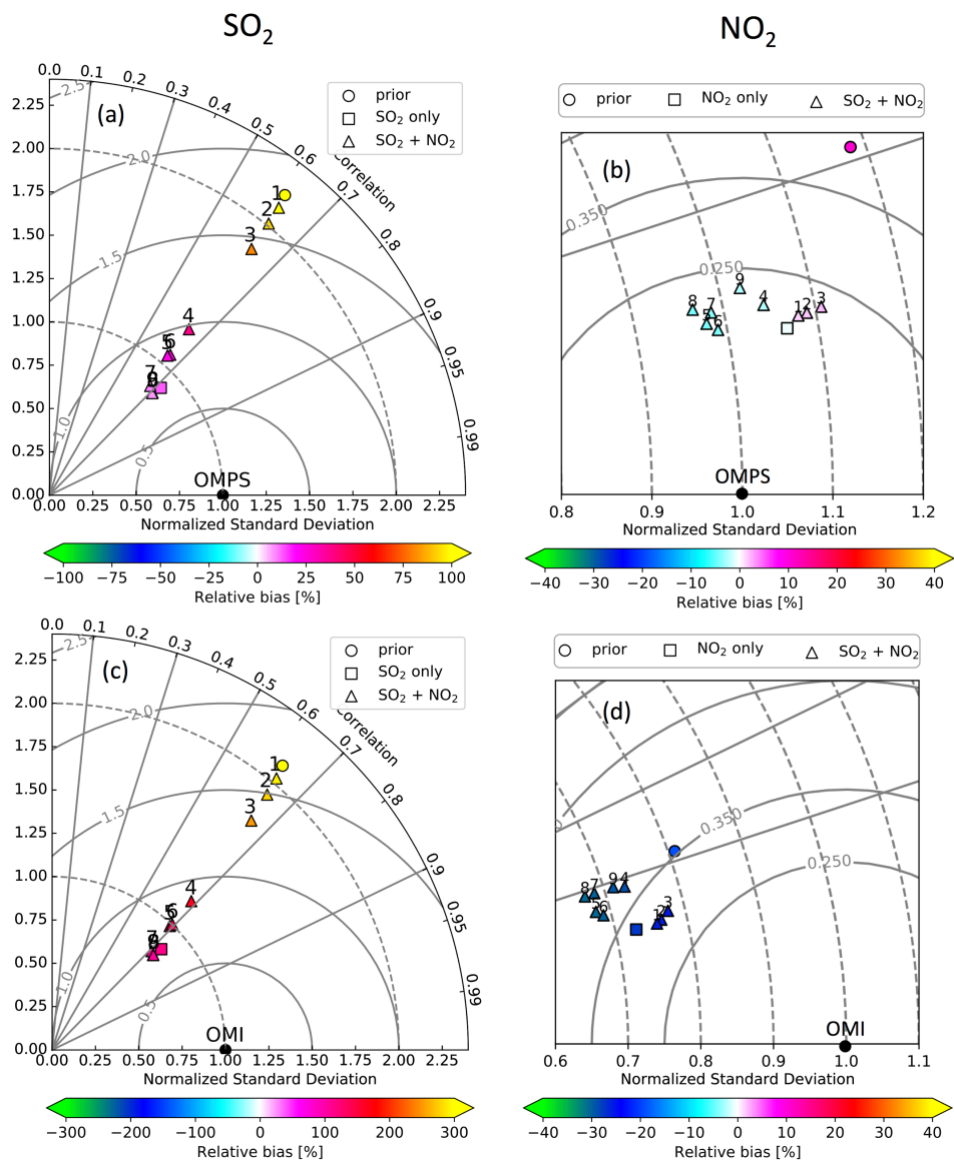
900

905



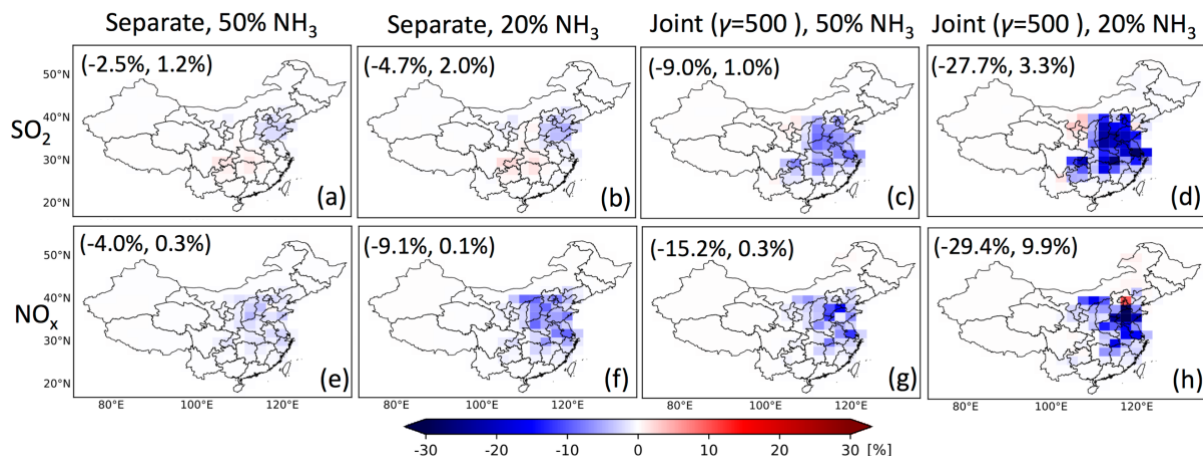
910 **Figure 7. SO<sub>2</sub> VCD in October 2013 from OMPS (a), prior GEOS-Chem simulation (b), posterior GEOS-chem simulation through using all OMPS data in the red box (c), and posterior GEOS-chem simulation through using only OMPS data that are in the grid cell where GEOS-Chem prior simulation of VCD is larger than 0.1 DU. For posterior simulation, we only plot SO<sub>2</sub> VCD over grid cells where OMPS data are used to constrain emissions. M and S point to a grid cell in Inner Mongolia and Sichuan basin, respectively.**

915



920 **Figure 8.** Taylor diagram of comparing GEOS-Chem simulation with OMPS (a for SO<sub>2</sub> and b for NO<sub>2</sub>) or OMI (c for SO<sub>2</sub> and d for NO<sub>2</sub>) in October 2013. Circles, squares, and triangles represent GEOS-Chem simulations using prior MIX 2010 emissions, posterior emissions constrained by single species (E\_SO2 for a and c, E\_NO2 for b and d), and posterior emissions constrained through joint inversion (E\_joint), respectively. Different triangles labeled by numbers represent different  $\gamma$  values in Eq. (1), and 1 through 9 correspond to 20, 50, 100, 200, 300, 500, 1000, 1500, and 2000, respectively.

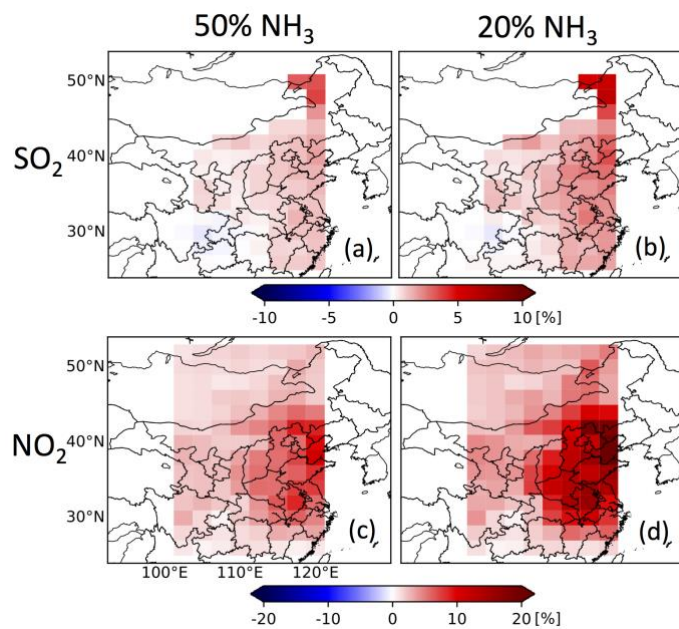




925

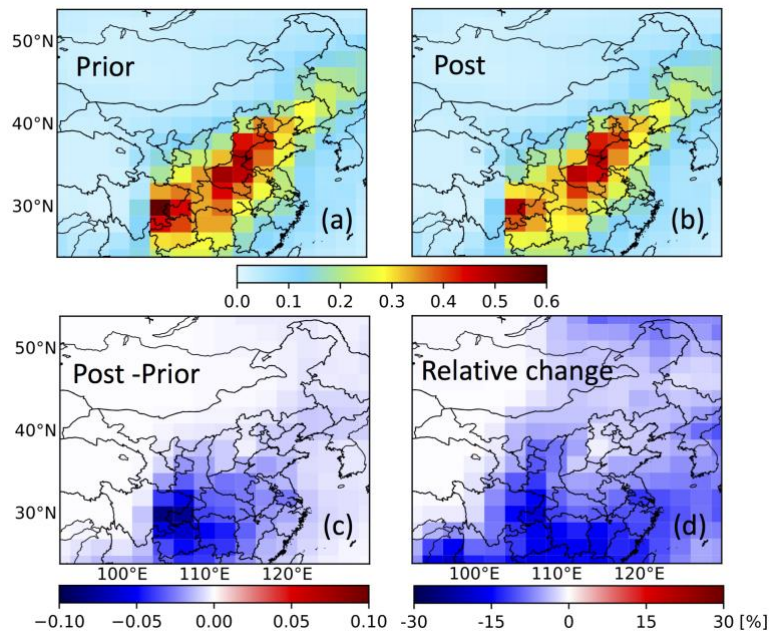
Figure 9. Relative changes of posterior SO<sub>2</sub> (top row) and NO<sub>x</sub> (bottom row) emissions from the scenarios of perturbing NH<sub>3</sub> emissions with respect to that using original NH<sub>3</sub> emission inventory. (a) and (b) are relative changes of posterior SO<sub>2</sub> emissions from E-SO<sub>2</sub>-0.5NH<sub>3</sub> and E-SO<sub>2</sub>-0.2NH<sub>3</sub> with respect to that from E-SO<sub>2</sub>, respectively. (c) and (d) are relative changes of posterior SO<sub>2</sub> emissions from E-joint-0.5NH<sub>3</sub>- $\gamma$ 500 and E-joint-0.2NH<sub>3</sub>- $\gamma$ 500 with respect to that from E-joint- $\gamma$  ( $\gamma=500$ ), respectively. (e) and (f) are relative changes of posterior NO<sub>x</sub> emissions from E-NO<sub>2</sub>-0.5NH<sub>3</sub> and E-NO<sub>2</sub>-0.2NH<sub>3</sub> with respect to that from E-NO<sub>2</sub>, respectively. (g) and (h) are similar to (c) and (d), respectively, but for posterior NO<sub>x</sub> emissions. Minimum and maximum are shown in brackets.

930



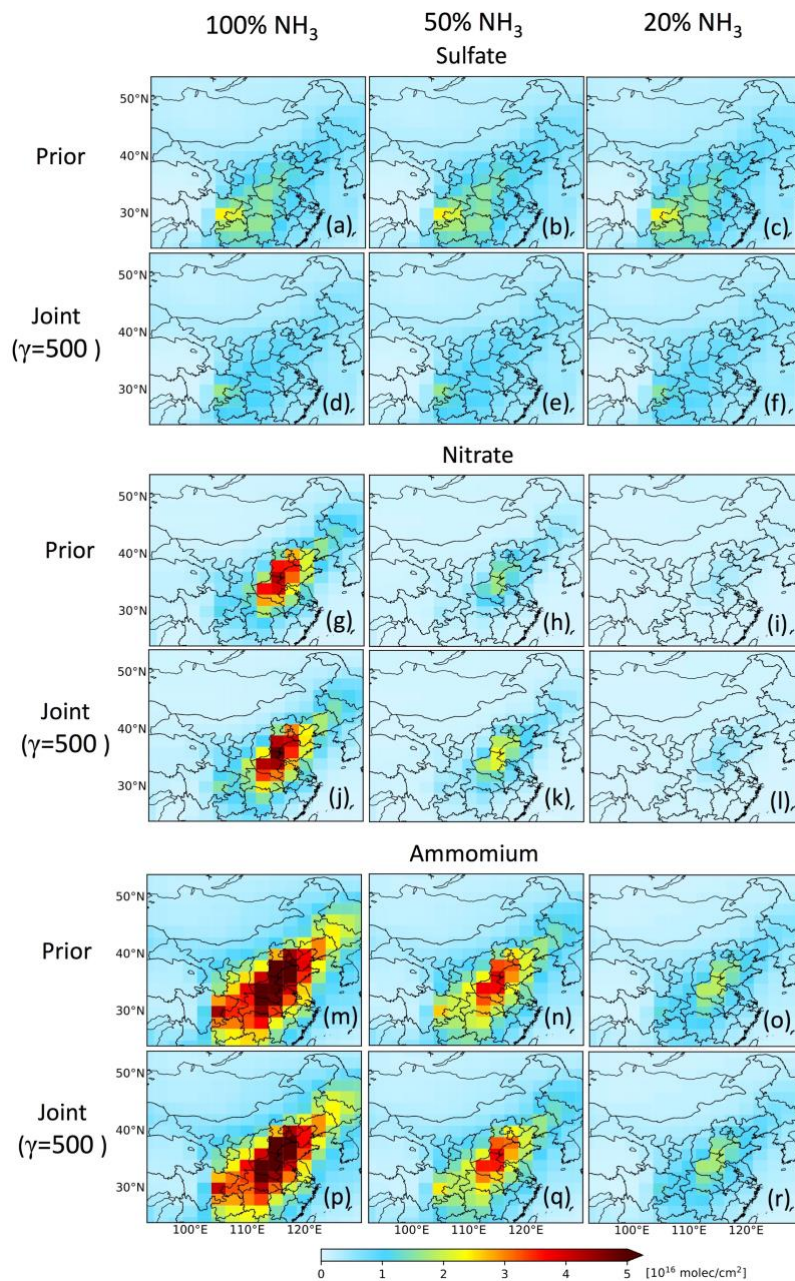
935

**Figure 10.** Relative change of GEOS-Chem SO<sub>2</sub> VCDs when NH<sub>3</sub> emissions reduce to 50% (a) and 20% (b), respectively at OMPS overpassing time. (c) and (d) are similar to (a) and (b), respectively, but for NO<sub>2</sub>.



940

**Figure 11. Sulfate-nitrate-ammonium aerosol optical depth in prior (a) and posterior joint inversion ( $\gamma=500$ ) (b). (c) is the difference between (b) and (a), and (d) is relative change in percentage.**



945 **Figure 12.** Sulfate, nitrate, and ammonium column loadings in different scenarios. (a), (b), and (c) are prior sulfate at 100%, 50%, and 20%  $\text{NH}_3$  emissions, respectively. (d), (e), and (f) are posterior sulfate from joint inversions ( $\gamma=500$ ) at 100%, 50%, and 20%  $\text{NH}_3$  emissions, respectively. (g)-(i) and (m)-(r) are similar to (a)-(f), but for nitrate and ammonium, respectively.